NASA-CR-195097

NAG9-593

IN-32-CR
11757
P-71

20 GHz Circularly Polarized, High Temperature Superconducting Microstrip Antenna Array

Jarrett D. Morrow
Jeffery T. Williams
Stuart A. Long
John C. Wolfe

(NASA-CR-195097) THE 20 GHz
CIRCULARLY POLARIZED, HIGH
TEMPERATURE SUPERCONDUCTING
MICROSTRIP ANTENNA ARRAY Final
Report (Houston Univ.) 71 p

N94-33083

Unclas

G3/32 0011757

A final report submitted to the
National Aeronautics and Space Administration
Johnson Space Center
Houston, Texas

Technical Report Number 94-13

Submitted to NASA May 31, 1994

Applied Electromagnetics Laboratory
Department of Electrical Engineering
University of Houston

TABLE OF CONTENTS

Project Summary

The primary goal of this study was to design and characterize a 4-element 20 GHz, circularly polarized microstrip patch antenna fabricated from $YBa_2Cu_3O_x$ superconductor. The purpose of the study is to support a high temperature superconductivity flight communications experiment between the Space Shuttle orbiter and the ACTS satellite. This study is intended to provide information into the design, construction, and feasibility of a circularly polarized superconducting 20 GHz downlink or cross-link antenna.

We have demonstrated that significant gain improvements can be realized by using superconducting materials for large corporate fed array antennas. In addition, we have shown that when constructed from superconducting materials, the efficiency, and therefore the gain, of microstrip patches increases if the substrate is not so thick that the dominant loss mechanism for the patch is radiation into the surface waves of the conductor-backed substrate.

We have considered two design configurations for a superconducting 20 GHz 4-element circularly polarized microstrip antenna array. The first is the Huang array that uses properly oriented and phased linearly polarized microstrip patch elements to realize a circularly polarized pattern. The second is a gap-coupled array of circularly polarized elements. In this study we determined that although the Huang array operates well on low dielectric constant substrates, its performance becomes extremely sensitive to mismatches, inter-element coupling, and design imperfections for substrates with high dielectric constants.

For the gap-coupled microstrip array, we were able to fabricate and test circularly polarized elements and 4-element arrays on $LaAlO_3$ using sputtered copper films. These antennas were found to perform well, with relatively good circular polarization. In addition, we realized a 4-element $YBa_2Cu_3O_x$ array of the same design and measured its pattern and gain relative to a room temperature copper array. The patterns were essentially the same as that for the copper array. The measured gain of the YBCO antenna was greater than that for the room temperature copper design at temperatures below $82K$, reaching a value of 3.4 dB at the lowest temperatures.

CHAPTER 1

Introduction

In the seven years since the discovery of high temperature superconductivity, dramatic technological break-throughs have been made in the development of these materials, led by advances in the deposition of high temperature superconducting (HTS) thin films on relatively low loss substrate materials. High quality superconducting transmission lines, filters, and resonators have been developed [1-3], and recently superconducting antennas with enhanced efficiencies have been demonstrated [4-13]. The success of these devices and the rapid maturation of deposition and etching technologies have made the near term application of high temperature superconducting devices in high frequency systems plausible.

The use of superconductors in the construction of passive antennas does not, in general, affect their radiation characteristics. These characteristics are usually associated with the physical construction of the antenna and, therefore, the antenna's radiation pattern and directivity will be unaffected by the use of superconducting materials. This independence implies that the radiation resistance and external reactance of the antenna will also be independent of the conducting material. Superconductors do, however, affect the input impedance, radiation efficiency, and frequency behavior of particular types of antennas. These changes are a result of the reduction in ohmic loss and the contributions of the internal reactance, which is directly associated with the effective penetration depth of the fields into the superconductor.

For the most part, the primary advantage of using superconducting materials in antenna systems is the reduction of the loss associated with transmission line matching circuits and feed networks, particularly at microwave and millimeter-wave frequencies where the ohmic losses begin to significantly affect the system performance. For large antenna arrays with long, elaborate corporate feed networks, the use of HTS transmission lines can substantially increase the gain of the antenna [14]. These benefits become more apparent as the number of radiating elements in the array increases. In later sections, we will show specific examples for microstrip corporate feed structures.

In addition to the feed line losses, we must also include the losses associated with the individual radiators to obtain the overall efficiency of the antenna array. In general, the efficiency of a microstrip patch antenna is limited by the power dissipated by ohmic losses in the patch element and the ground plane, dielectric loss in the supporting substrate, and undesirable excitation of surface-wave radiation. The level of surface wave excitation increases with increasing substrate thickness and dielectric constant. For this reason, in many designs, the substrate upon which the microstrip antenna is patterned is electrically thin (less than $0.01\lambda_o$). On these thin substrates, the coupling into the surface waves is reduced. Unfortunately, this benefit is often countered by a substantial decrease in the impedance bandwidth and the antenna efficiency due to conductor and dielectric loss. These losses can be significantly reduced by constructing the antenna from thin films of high temperature superconductor on low loss substrates since high quality HTS materials have microwave surface resistances that are one to two orders of magnitude less than that of copper at 77K. Properly designed microstrip antennas and antenna arrays show marked improvement in their antenna efficiencies when constructed from high quality HTS films [11,12].

The primary goal of this study was the design and characterization of a 2x2 Ka-band (20 GHz) circularly-polarized microstrip patch antenna array constructed of $YBa_2Cu_3O_x$ superconductor. This effort was intended to support a high temperature superconductivity (HTSC) flight communications experiment between the Space Shuttle orbiter and the Advanced Communications Technology Satellite (ACTS), a project which is a joint venture of the Johnson Space Center and Lewis Research Center. In this report, we will discuss the application of superconductors in microstrip transmission line feed networks and microstrip patch antennas. We will show how the use of HTS materials can improve the gain of microstrip antenna arrays. We will then consider two potential designs for a circularly polarized HTS microstrip patch array. The first design uses combinations of linearly polarized elements to generate circular polarization, whereas, the second design uses an array of circularly polarized elements. Finally, we will present some results from our experimental investigation of these circularly-polarized designs.

CHAPTER 2

Superconducting Microstrip Antennas

In this chapter we will discuss some of the fundamental properties of superconducting microstrip transmission lines and rectangular microstrip patch antennas. In the first section we will examine the efficiency of normally conducting and superconducting corporate microstrip antenna feed networks. This section is followed by a discussion of the efficiency and bandwidth of microstrip patch antennas. The final section briefly describes the results obtained in other investigations of linearly polarized HTS microstrip antennas and arrays.

2.1: Feed Line Losses

As previously mentioned, the primary advantage of using superconducting materials in antenna systems is the reduction of the loss in large transmission line feed networks, particularly at high frequencies where the ohmic losses of normal conductors are quite large. We will demonstrate this for the corporate-fed square array of linearly polarized, printed dipole elements shown in Fig. 2.1. This example well represents the transmission line losses associated with other square arrays with different microstrip antenna elements. We will assume that each element is matched to its corresponding feed line and that the radiation efficiency of each element is 100%. In addition, we will also assume a uniform array where all of the elements are excited with equal amplitude and equal phase.

For an array such as that shown in Fig. 2.1 the number of antenna elements on a side is 2^N. Therefore, the total number of elements in the array is 2^{2N}. Given our stated assumptions it is straightforward to determine that the efficiency of this array, which only has loss in the transmission line feed network, is

$$\eta \approx e^{-2\alpha d\left(N+\sum_{i=0}^{N-1} 2^i\right)}, \tag{2.1}$$

where α is the attenuation constant [nepers/m] for the microstrip feed lines. Obviously, α will be different for the different impedance sections of microstrip in the feed network.

However, for this demonstration we will assume that it is the constant attenuation associated with a 50 Ω line. (The expressions used for the microstrip attenuation constant are those given in [15].) The overall gain (G) of the antenna array is given in terms of the efficiency as

$$G = \eta D, \tag{2.2}$$

where D is the directivity of the array. When expressed in dB, (2.1) and (2.2) are

$$\eta^{dB} \approx -20\ \alpha d \left(N + \sum_{i=0}^{N-1} 2^i \right) \log(e) \tag{2.3}$$

and

$$G^{dB} = \eta^{dB} + D^{dB}. \tag{2.4}$$

The efficiency of a 20 GHz corporate microstrip feed as a function of the number of array elements is shown in Fig. 2.2. In this example we assume that the element spacing is $\lambda_o/2$, and the substrate is assumed to be 0.010 [in] thick $LaAlO_3$, with a relative permittivity of 23 and a loss tangent of 1×10^{-5}. The results in Fig. 2.2 are representative of microstrip fabricated from copper and $YBa_2Cu_3O_x$ superconductor. At room temperature ($300K$) the copper is assumed to have a conductivity of 5.8×10^7 [S/m] and a value of 40×10^7 [S/m] at $77K$. The classical two-fluid model [16] is used to characterize the $YBa_2Cu_3O_x$ superconductor. This empirical model is valid for HTS superconductors when the magnetic fields within the material are weak, such that it is in the pure superconducting state. In this model the superconductor is represented by a complex conductivity, given by

$$\sigma_{sc} = \sigma_1 - j\sigma_2, \tag{2.5}$$

where the real and negative imaginary parts are expressed as

$$\sigma_1 = \sigma_n \left(\frac{T}{T_c} \right)^4 \tag{2.6}$$

and

$$\sigma_2 = \frac{1}{\omega \mu_o \lambda^2(0)} \left[1 - (T/T_c)^4 \right]. \tag{2.7}$$

For a high quality $YBa_2Cu_3O_x$ thin film, the normal state conductivity σ_n is approximately equal to 2×10^6 [S/m], the zero temperature effective penetration depth $\lambda(0)$ is 0.150 [μm], and the critical temperature T_c is $90K$. In these expressions T is the operating temperature in Kelvin. The temperature dependence of the two-fluid model for high temperature superconductors is presently unsettled and is a matter of much debate. For our purposes we have decided to use the classical BCS temperature dependence. Certainly, this choice does not impact the qualitative nature of our results.

From Fig. 2.2 we notice that as the number of elements in the array increases the efficiency of the copper arrays decreases noticeably. On the other hand, the efficiency for the YBCO array remains nearly constant on this scale. For modest quality $YBa_2Cu_3O_x$ thin films the efficiency will be less than that shown in this example, but it will remain well above that of the copper arrays. This example also demonstrates that the increase in efficiency realized by using a $YBa_2Cu_3O_x$ feed network only becomes appreciable when the number of array elements is large. Therefore, due to the scale limitations of present $YBa_2Cu_3O_x$ thin film fabrication technology a large HTS feed network is only feasible for high frequency arrays. But we must also keep in mind that these results only represent the efficiency of the feed network, which is single component of the overall efficiency for the antenna system. To obtain the overall efficiency we must also account for losses in the other components of the system, in particular the antenna elements. This is the subject of the next section.

2.2: Microstrip Antennas

In addition to the losses in the transmission line feed network we must also take into account the energy lost by the microstrip patch antennas into mechanisms other than radiation into space. In this section we will examine how these losses affect the antenna efficiency and bandwidth of rectangular microstrip patch antennas.

The antenna efficiency of a microstrip antenna (Fig. 2.3) can be expressed in terms of the power lost due to ohmic heating in the dielectric (P_d) and conductors (P_c) of the structure, radiation into surface waves (P_{sw}), and radiation into space (P_{sp}). In terms of these quantities we define the antenna efficiency η_a as

$$\eta_a = \frac{P_{sp}}{P_{in}} = \frac{P_{sp}}{P_{sp} + P_{sw} + P_d + P_c}, \tag{2.8}$$

where P_{in} is the total input power. The antenna efficiency can also be expressed in terms of the individual quality factors of the resonant microstrip antenna. First, we will define the total quality factor for the antenna (Q) as

$$Q = \frac{\omega_o U_S}{P_{in}}, \tag{2.9}$$

where U_S is the total energy stored by the antenna and ω_o is the resonant angular frequency. Similarly, we can write a general expression for the individual dielectric, conductor, surface wave, and space wave quality factors as

$$Q_x = \frac{\omega_o U_S}{P_x}, \tag{2.10}$$

where $x = d,\ c,\ sw,$ or sp. Thus, the total quality factor is given as

$$\frac{1}{Q} = \frac{1}{Q_{sp}} + \frac{1}{Q_{sw}} + \frac{1}{Q_c} + \frac{1}{Q_d}. \tag{2.11}$$

Combining (2.9)-(2.11) with (2.8) we obtain

$$\eta_a = \frac{Q}{Q_{sp}}. \tag{2.12}$$

It is obvious from these expressions that the overall efficiency of a microstrip antenna is increased by increasing the percentage of power radiation into space.

To obtain a measure of the amount of the total radiated power that is lost to radiation into the surface waves, we define the radiation efficiency of a microstrip antenna η_r as

$$\eta_r = \frac{P_{sp}}{P_{sp} + P_{sw}}. \tag{2.13}$$

As shown in [17], the radiation efficiency for a rectangular microstrip patch is approximately equal to that of a horizontal electrical dipole (η_r^d). Therefore,

$$\eta_r \approx \eta_r^d = \frac{4c_1}{4c_1 + 6\pi^2\mu_r(\frac{t}{\lambda_o})\left(1 - \frac{1}{n^2}\right)^3}, \tag{2.14}$$

where n is the refractive index of the substrate ($n = \sqrt{\mu_r \epsilon_r}$) and

$$c_1 = 1 - \frac{1}{n^2} + \frac{2}{5n^4}. \tag{2.15}$$

The radiation efficiency can also be expressed in terms of a radiation quality factor Q_R as

$$\eta_r = \frac{Q_R}{Q_{sp}}. \tag{2.16}$$

For a rectangular microstrip patch antenna Q_R is given by [18]

$$Q_R = \left(\frac{1}{Q_{sp}} + \frac{1}{Q_{sw}}\right)^{-1} = \eta_r \frac{3\epsilon_r(W/L)}{16c_1(t/\lambda_o)}. \tag{2.17}$$

Therefore, from (2.16) and (2.17)

$$Q_{sp} = \frac{3\epsilon_r(W/L)}{16c_1(t/\lambda_o)} \tag{2.18}$$

and

$$Q_{sw} = \frac{Q_R}{1 - \eta_r}. \tag{2.19}$$

The dielectric and conductor quality factors can be determined from the cavity model for a rectangular microstrip patch antenna. The dielectric Q is given simply by

$$Q_d = \frac{1}{\tan\delta}, \tag{2.20}$$

where $\tan\delta$ is the loss tangent of the dielectric substrate. The conductor Q is

$$Q_c = 120\pi^2 \mu_r (t/\lambda_o) \left(\frac{2}{R_s^{grd} + R_s^{pat}} \right), \tag{2.21}$$

where R_s^{grd} and R_s^{pat} are the surface resistances of the ground plane and patch conductors, respectively. The equations (2.17-2.21) are substituted into (2.12) to obtain the total antenna efficiency.

In addition to the antenna efficiency, we can also express the impedance bandwidth (VSWR$<$ 2) as a function of the total quality factor of the antenna and the resonant frequency f_o. From [18], this impedance bandwidth is

$$BW = \frac{f_o}{Q\sqrt{2}}. \tag{2.22}$$

In Figures 2.4 and 2.5 we have plotted the antenna efficiency and impedance bandwidth, respectively, as a function of normalized substrate thickness for 3 different microstrip cases. Each represents a 20 GHz rectangular microstrip patch with an aspect ratio (W/L) of 1.5, on a $LaAlO_3$ substrate with a dielectric constant of 23 and a loss tangent of 1×10^{-5}. We have assumed that for each antenna the ground plane and the patch are constructed from the same material. For the copper antennas at $300K$ and $77K$ the surface resistances used correspond to conductivities of 5.8×10^7 [S/m] and 40×10^7 [S/m], respectively. The expression for the surface resistance is given by

$$R_s = \sqrt{\frac{\omega\mu}{2\sigma}}. \tag{2.23}$$

For the $YBa_2Cu_3O_x$ antenna the parameters of the two-fluid model described in the previous section are assumed. The resulting surface resistance is 0.1424 [mΩ] at $77K$. This value is consistent with that for the very best $YBa_2Cu_3O_x$ films.

From Fig. 2.4 we observe that for very thin substrates the antenna efficiency is small, limited by the ohmic losses of the conductors and the dielectric losses. Since the conductor losses are quite high for the copper antennas the efficiencies for these antennas are small for thin substrates. In contrast, we notice that the efficiency for the $YBa_2Cu_3O_x$ antenna is relative high for the thinner substrates. The efficiency for this superconducting antenna is primarily a function of the dielectric loss tangent. For each antenna the efficiency increases as the thickness increases. The efficiency for the superconducting antenna reaches a maximum at approximately $t/\lambda_o = 0.003$, while the maximum for the copper antennas is reached for t/λ_o greater than 0.02. At the maximum, the space wave radiation is the dominant loss mechanism. Beyond these corresponding maxima, the loss of energy due to radiation into the TM_0 surface wave of the conductor-backed substrate becomes significant. For the thicker substrates the surface-wave loss becomes the dominant loss mechanism for each antenna, and as a result the efficiencies for the individual antenna become approximately equal. These plots clearly demonstrate that as the thickness of the substrate increases, the surface-wave loss increases. An extensive study of the characteristics of microstrip patch antennas on thin substrates is presented in our previous report to NASA [19].

The plots for the impedance bandwidth shown in Fig. 2.5 demonstrate that, in general, the bandwidth increases with increasing substrate thickness. The only exception occurs when the antenna has a very low efficiency due to extreme conductor loss. In this region the impedance bandwidth actually increases with increasing loss (decreasing substrate thickness). This characteristic is similar to that for other antennas when the radiation loss becomes small relative to the ohmic losses.

2.3: Previous Investigations

To our knowledge no one has successfully designed and constructed an HTS circularly-polarized microstrip array. In fact, only a few studies have been conducted to investigate the performance of HTS materials in conventional linear microstrip elements and array designs. The most notable studies whose results pertain to this investigation are briefly discussed here.

Herd, et. al. [8,9] have designed and constructed a 12 GHz, 16 element microstrip array with a proximity coupled YBCO feed network. The structure consists of 16 silver rectangular microstrip patches printed on a quartz substrate that also functions as a window for the vacuum enclosure of the cryo-chamber. This substrate is separated from the YBCO feed network by a vacuum gap. The feed network is patterned on a $LaAlO_3$ substrate with a silver ground plane. Small microstrip patches on the $LaAlO_3$ substrate are used to electromagnetically couple with the larger patches on the quartz. The results reported from this study are limited to a demonstration of the coupling of energy into the array over an approximately 8% bandwidth and a relatively high directivity pattern. The scanning of the main beam has also been demonstrated by using a built-in phase taper in the feed network. No results have been reported concerning the efficiency or relative gain of the antenna with respect to a similar antenna constructed with a normally conducting feed network. To achieve a relatively high bandwidth the structure was electrically thick. As a result, surface wave interactions, which are incorporated in the design assuming that the array is infinite, become severe. In particular, this study does not address the potentially deleterious effects of surface wave scattering from the edges of the finite structure. We suspect that these effects will be quite large. All the measured results were performed in a waveguide simulator which allows for the simulation of an infinite structure, thereby eliminating the edge scattering effects.

In a study previously reported to NASA-JSC [19], Smith, et. al. have investigated the use of HTS materials to improve the efficiency of microstrip antennas on electrically thin dielectric substrates. For many monolithic applications, particularly integrated applications, the supporting substrate is very thin, less than $0.02\lambda_o$. As shown in Fig. 2.4, the efficiencies of normally conducting microstrip patches become quite small in this range. Smith, et. al. demonstrated theoretically that the use of superconducting materials could significantly increase the efficiency of such antennas. Using a 4.9 GHz patch on a 0.020 [in] $LaAlO_3$ substrate, Smith, et. al. successfully verified their theoretical predictions. They developed a modified Wheeler end-cap technique to accurately measure the efficiency of microstrip elements and used this technique to measure efficiencies of approximately 97% and 77% for YBCO and copper patches, respectively, at $77K$. These results compare well with the predicted values of 96% and 75%. In addition, this study included the development of a effective coplanar waveguide feed for microstrip patch elements suitable for monolithic microwave and millimeter-wave applications.

The most comprehensive study into the design of linear HTS microstrip elements and arrays has been presented in [4,5,6,10]. The entirety of this investigation is summarized in [7]. In this work, three 30 GHz microstrip designs in both single element and 4-element array configurations were investigated. The designs studied included patches that are directly coupled, gap-coupled, and electromagnetically coupled to the feed line. Rectangular patches were exclusively used in the directly coupled designs, and both rectangular and circular patches were investigated in the gap and electromagnetically coupled cases. In addition, the characteristics of a 64-element, 30 GHz linearly polarized microstrip array designed and fabricated by Ball Aerospace Systems Division were measured. The experimental results obtained in this investigation are consistent with the predictions presented in the earlier sections. In particular, for a 30 GHz directly coupled rectangular patch ($W/L = 1.75$) on a 0.010 [in] $LaAlO_3$ substrate with a copper ground plane they measured a $77K$ efficiency of approximately 87%, which was compared to a measured efficiency of 78% for a gold element at the same temperature. The bandwidth of these elements was found to be less than 1%. Using these elements in a uniform 4-element linearly polarized array, the relative gain at $77K$ with respect to a gold array at $77K$ was measured to be approximately 0.13 dB. With respect to the gold array at room temperature ($300K$) the relative gain was approximately 1 dB. For the 64 element array the relative gain with respect to an equivalent gold array at $77K$ and $300K$ was determined to be approximately 2.0 dB and 4.8 dB, respectively.

Our intent in the remaining sections of this report is to build upon this base of knowledge by investigating the properties of circular polarized 4-element microstrip arrays constructed with superconducting material.

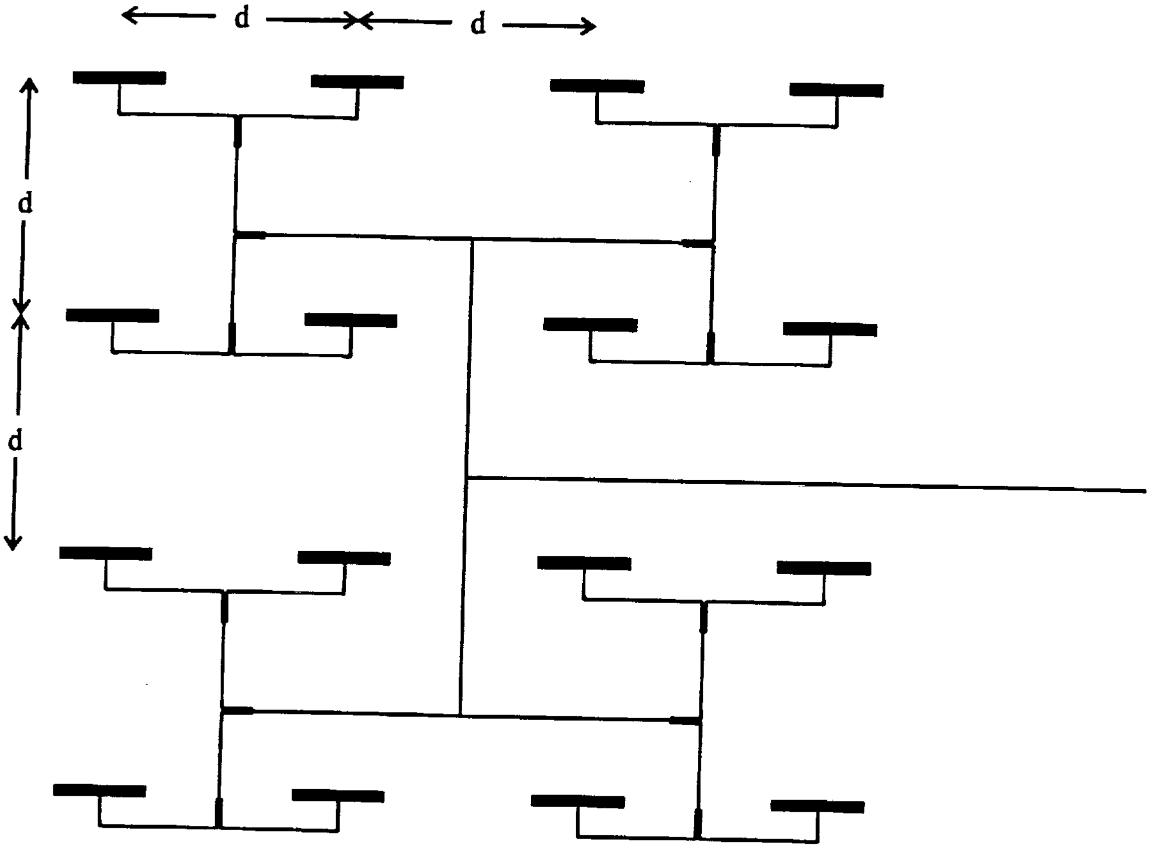

Figure 2.1: An example of a $2^N \times 2^N$ ($N = 2$) corporate-fed square array.

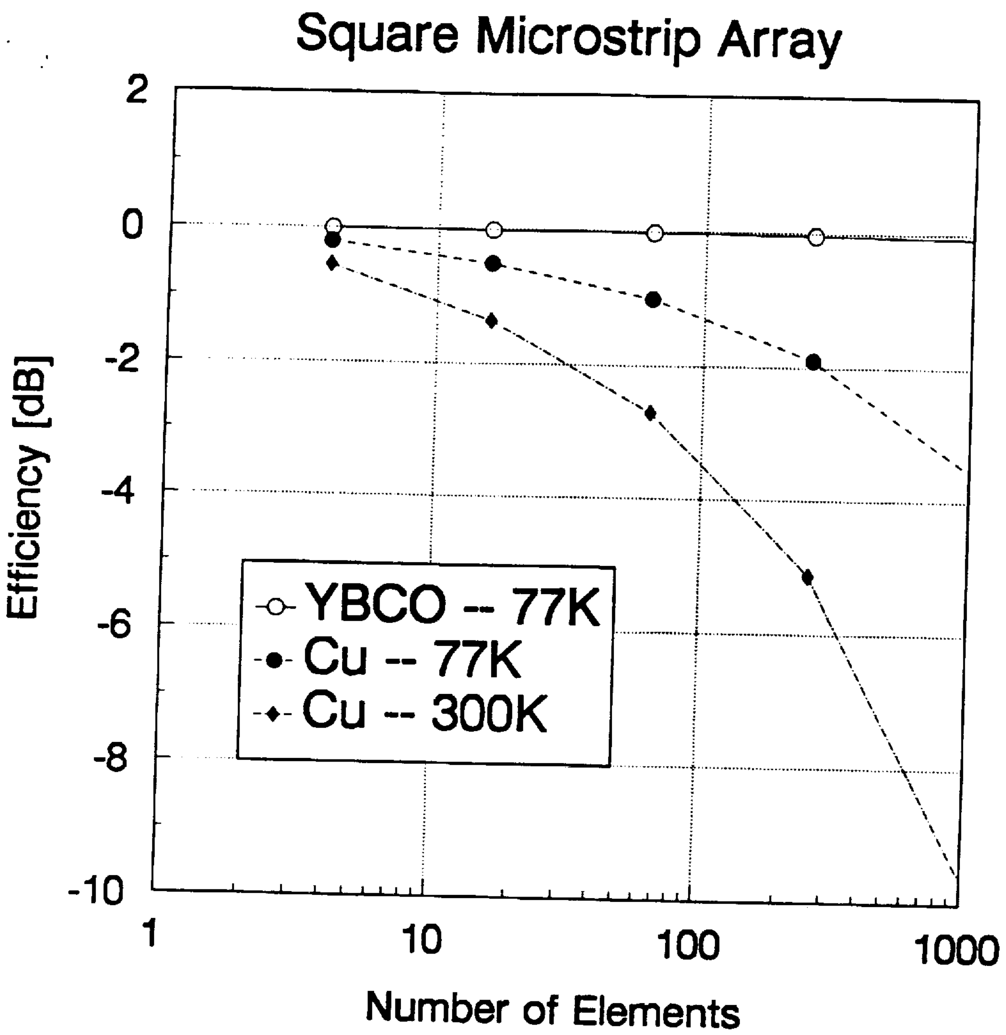

Figure 2.2: Efficiency for a 20 GHz square, microstrip fed array on $LaAlO_3$ ($\epsilon_r = 23$, $\tan\delta = 10^{-5}$).

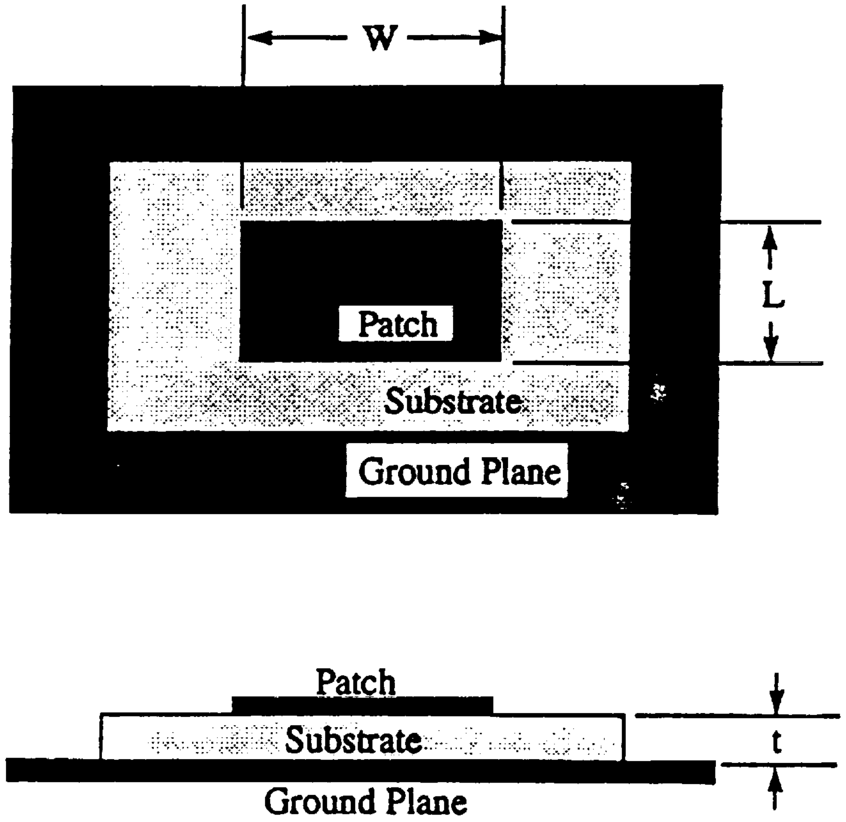

Figure 2.3: Geometry for a rectangular microstrip patch antenna.

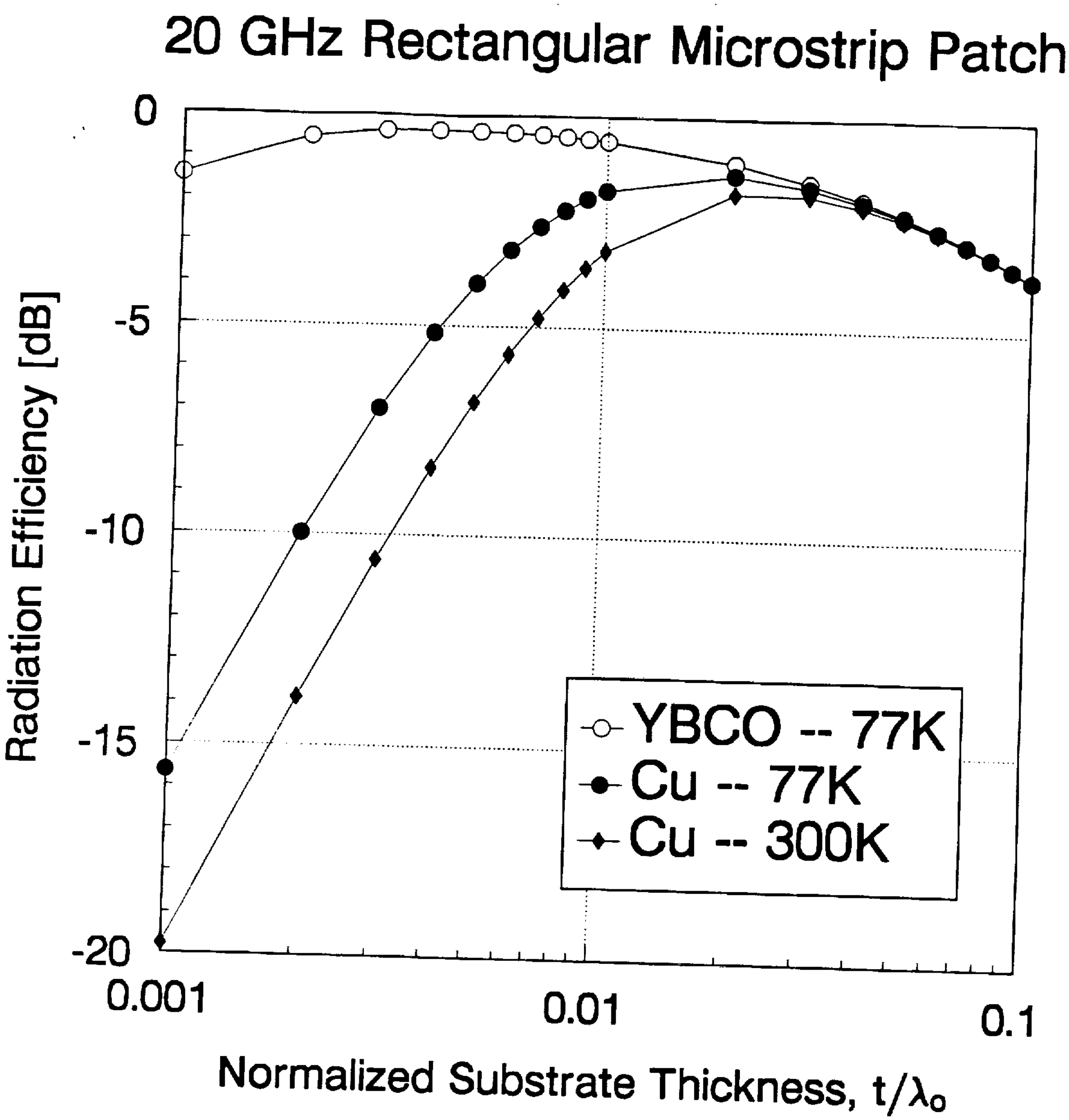

Figure 2.4: Antenna efficiency for a 20 GHz rectangular microstrip antenna on $LaAlO_3$ ($\epsilon_r = 23$, $\tan\delta = 10^{-5}$).

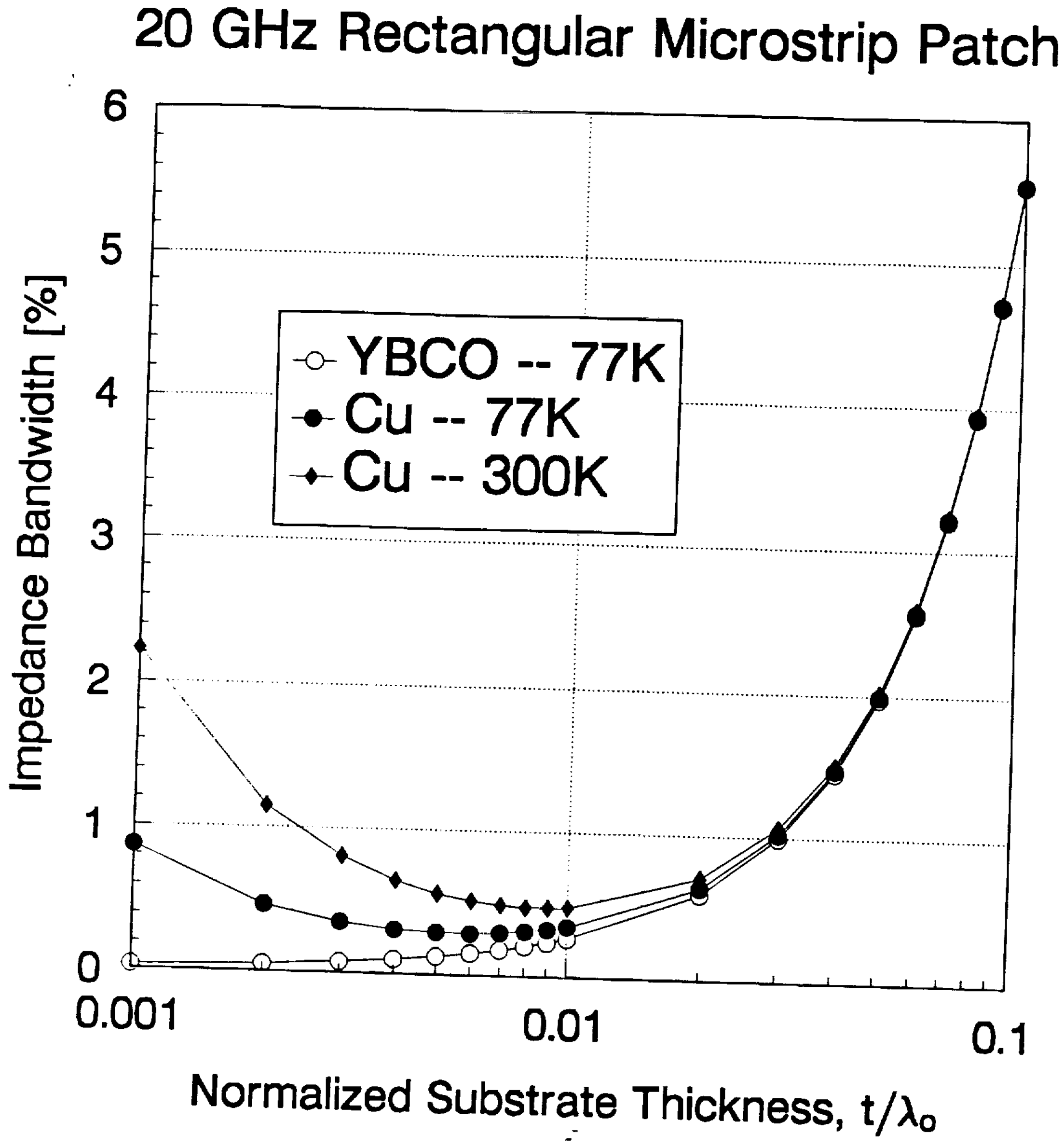

Figure 2.5: Impedance bandwidth for a 20 GHz rectangular microstrip antenna on $LaAlO_3$ ($\epsilon_r = 23$, $\tan\delta = 10^{-5}$).

CHAPTER 3

Circularly-Polarized Superconducting Microstrip Antennas

The design of HTS circularly-polarized microstrip antennas is complicated by the cryogenic environment and the properties of the superconducting and substrate materials. In this chapter we will discuss some of the design issues associated with the conductor and substrate materials. Two different circularly-polarized array configurations will be presented and their radiation properties determined using analysis to be presented.

3.1: Design Considerations

There are many significant issues that must be considered when designing a circular-polarized HTS microstrip antenna array. The most prominent are related to the dielectric substrate. At present, the substrate material that best satisfies all of the electrical requirements (low loss, reasonable dielectric constant) and on which very high quality $YBa_2Cu_3O_x$ thin films can be grown is $LaAlO_3$. $LaAlO_3$ has a good lattice match with YBCO, therefore the films grown on these substrates are highly oriented, have fewer grain boundaries, and are more uniform that those grown on other microwave compatible substrate materials. As a result, good $YBa_2Cu_3O_x$ films on $LaAlO_3$ substrates have low surface resistances (typically less than 0.5 [mΩ] at 20 GHz, $77K$) and high transition temperatures (greater than 89-90K). Unfortunately, $LaAlO_3$ is far from being an ideal substrate material. It has a relatively high dielectric constant ($\epsilon_r \approx 19-25$) for microwave and antenna applications. It is extremely fragile and difficult to machine. In addition, $LaAlO_3$ is subject to a high degree of twinning which weakens the substrate and is often blamed for introducing loss in the HTS films because the twinning is reflected in the film causing weak links and grain boundaries. To make matters worse $LaAlO_3$ experiences a phase transition at the temperatures required for the deposition of the $YBa_2Cu_3O_x$ material. Thus, the characteristics of the substrate often change during the deposition process. Another result of the high degree of twinning is that the dielectric constant of $LaAlO_3$ varies not only from sample to sample, but even over an individual substrate. Reported values of the dielectric constant for $LaAlO_3$ range from 19 to 25, although most accept a value of between 23 and 25. This uncertainty and variation in the dielectric constant of $LaAlO_3$ causes uncertainty and variation in the resonant frequency of and efficient coupling to microstrip antennas fabricated on these substrates. $LaAlO_3$ does, however, have a relatively low loss tangent. The reported values range from approximately 10^{-4} to 10^{-6}. Several other competing substrate materials exist, but for various reasons (usually because films grown on them have higher surface resistances) have yet to gain universal acceptance. These include MgO, $NdGaO_3$, and r-plane Al_2O_3 (sapphire). The primary disadvantage of r-plane sapphire is that it is highly anisotropic.

The relatively high value of the dielectric constant of $LaAlO_3$ does allow for the miniaturization of microstrip devices, such as patch antennas. In an antenna array this results in more room between the radiators, thus allowing for more flexibility in the layout and the inclusion of other devices. However, as a consequence of the high ϵ_r the edge impedance of patch antennas becomes extremely high and the impedance bandwidth is reduced. Although it is difficult to accurately measure high values of edge impedance for a rectangular microstrip patch antenna, it is well over 1000 [Ω] for 0.010 [in] $LaAlO_3$ substrates. As a result, directly coupled feeds must be inset well into the patch. These significant inset distances therefore preclude construction of directly coupled circularly-polarized elements since such elements generally require orthogonally fed modes that would be significantly perturbed by large inset distances. These issues are also common to electromagnetically coupled feeds (excluding gap-coupled feeds) since they also have to be inset well underneath the patch when the substrate dielectric constant is large.

To help offset the reduced bandwidth resulting from the use of a high ϵ_r substrate material, the thickness of the substrate can be increased. This approach, however, has a significant drawback since increasing the substrate thickness also increases the coupling into the surface-wave modes of the conductor-backed dielectric layer. The effects of increased surface wave excitation are generally more serious than the reduced bandwidth. Designs with multiple layers of lower ϵ_r materials offer potential solutions to some of these problems; however, these designs are much more complicated and they present cooling problems since in practice it is difficult to ensure low loss thermal and electrical bonds between the layers.

3.2: Design Expressions

To aid in the design of the 4-element arrays we need techniques to readily calculate the radiation patterns. In this section we present the simple, closed-form design equations used in this study. To obtain these expressions, we use reciprocity to determine the radiated fields from a horizontal electric dipole. These fields are used, in effect, as the Green's functions to determine the element factors for the individual patch antennas. To obtain the closed-form design equations we assume that the current distribution on the individual patches is that of the dominant TM_{10} mode in the cavity model of the patch. The amplitude and phase of the mode is specified by the designer. This requires that the designer either neglect mutual coupling effects between the patches (which results in 1st order accuracy), or determine in some apriori fashion the effect of mutual coupling on the individual current distributions.

Figure 3.1 shows a diagram of a single rectangular microstrip patch antenna on a dielectric substrate of thickness t. For this study we assume that the substrate is non-magnetic, hence $\mu = \mu_o$. First, we will consider an $\hat{\mathbf{x}}$-directed horizontal electric dipole with a unity dipole moment located at the origin. The radiated electric field components determined using reciprocity are [20]

$$E_{\theta}^{h,x} = \left[\frac{-j\omega\mu_o}{4\pi r}e^{-jk_o r}\right] \cos\theta\cos\phi \left[\frac{2\tan\left(k_o t N(\theta)\right)}{\tan\left(k_o t N(\theta)\right) - \frac{j\epsilon_r}{N(\theta)}\cos\theta}\right] \tag{3.1}$$

and

$$E_{\phi}^{h,x} = \left[\frac{j\omega\mu_o}{4\pi r}e^{-jk_o r}\right] \sin\phi \left[\frac{2\tan\left(k_o t N(\theta)\right)}{\tan\left(k_o t N(\theta)\right) - \frac{jN(\theta)}{\mu_r}\sec\theta}\right], \tag{3.2}$$

where

$$N(\theta) = \sqrt{n^2 - \sin^2\theta}. \tag{3.3}$$

and n is the refractive index of the substrate ($n = \sqrt{\mu_r \epsilon_r}$). To obtain the element factors for a rectangular microstrip patch (element i) centered at $(x_i, y_i, 0)$, oriented with the E-plane parallel to the x-axis, we assume that the current density on the patch is

$$J_{x_i} = \cos\left((x - x_i)\frac{\pi}{L}\right), \qquad x \in [x_i + L/2, x_i - L/2],\ y \in [y_i + W/2, y_i - W/2]. \tag{3.4}$$

Integrating the dipole fields against this current density over the surface of the patch, we obtain the following expressions for the radiated far-fields of an $\hat{\mathbf{x}}$-oriented microstrip antenna:

$$E^{x}_{\theta_i} = E^{h,x}_{\theta}\ F_x(\theta,\phi) \tag{3.5}$$

and

$$E^{x}_{\phi_i} = E^{h,x}_{\phi}\ F_x(\theta,\phi), \tag{3.6}$$

where $k_x = k_o \sin\theta\cos\phi$, $k_y = k_o \sin\theta \sin\phi$, and

$$F_x(\theta,\phi) = \left[\frac{W\ e^{jk_y y_i}\sin\left(k_y \frac{W}{2}\right)}{k_y \frac{W}{2}}\right] \left[\frac{\frac{\pi L}{2}\ e^{jk_x x_i}\cos\left(k_x \frac{L}{2}\right)}{\left(\frac{\pi}{2}\right)^2 - \left(k_y \frac{L}{2}\right)^2}\right]. \tag{3.7}$$

The radiated far-fields for a $\hat{\mathbf{y}}$-oriented microstrip antenna (E-plane parallel to the y-axis) can be obtained from these expressions by simply interchanging y for x, W for L (L is always assumed to be the resonant dimension), $\cos\phi$ for $\sin\phi$, and $\sin\phi$ for $\cos\phi$.

To obtain the total fields radiated by an array of microstrip patch elements, we combine the individual fields represented by the previous equations. In doing so, we must specify the amplitude and phase for each patch. Thus, for a linear array of N_x $\hat{\mathbf{x}}$-oriented microstrip patches

$$E_\theta = \sum_{i=1}^{N_x} A_i e^{j\gamma_i} E^{x}_{\theta_i}(x_i, y_i) \tag{3.8}$$

and

$$E_\phi = \sum_{i=1}^{N_x} A_i e^{j\gamma_i} E^{x}_{\phi_i}(x_i, y_i), \tag{3.9}$$

where A_i and γ_i represent the amplitude and phase of the fields from the ith $\hat{\mathbf{x}}$-oriented element, respectively. Similarly, for a linear array of N_y $\hat{\mathbf{y}}$-oriented microstrip patches

$$E_\theta = \sum_{i=1}^{N_y} B_i e^{j\zeta_i} E^{y}_{\theta_i}(x_i, y_i) \tag{3.10}$$

and

$$E_\phi = \sum_{i=1}^{N_y} B_i e^{j\zeta_i} E^y_{\phi_i}(x_i, y_i), \tag{3.11}$$

where B_i and ζ_i represent the amplitude and phase of the fields from the ith $\hat{\mathbf{y}}$-oriented element, respectively. The total fields are obtained by adding (3.8) to (3.10) and (3.9) to (3.11).

3.3: Circularly-Polarized Array Designs

In this study, we have concentrated on 2 different circularly-polarized array designs. The first, which we deem as the Huang array, uses directly-coupled linear array elements combined in such as way as to realize circular-polarization [21]. This design, described in Sec. 3.3.1, is attractive for HTS applications since the feeds can be directly coupled to rectangular patch elements, thus taking advantage of the direct feed coupling, which is generally less sensitive to substrate variations, and the broader bandwidth and small cross-pole characteristics of rectangular microstrip patches. The second array design, a gap-coupled array (described in Sec. 3.3.2), uses square patch elements that are feed orthogonally, with a 90^o phase differential, by gap-coupled feed lines. Although gap-coupled feeds are generally more sensitive to substrate permittivity variations, this array design is attractive since each element is circularly-polarized, thereby reducing the sensitivity of the total pattern to weakly excited elements, and, in general, this design has a more desirable radiation pattern.

3.3.1: Huang Array

In this section we will briefly describe a 4-element microstrip array, originally reported by Huang [21], that generates circular polarization using single-feed linearly polarized elements. A schematic representation of the basic array is shown in Fig. 3.2. From this figure, we observe that the relative orientation of the patches in conjunction with the phasing of the feeds creates a circularly-polarized field at broadside. Away from broadside the quality of the circular polarization degrades. By using single-feed elements the overall complexity of the feed network is reduced, and due to the relative orientations of neighboring elements the mutual coupling is reduced as compared to a typical square array. These features are very appealing for HTS array design on high permittivity $LaAlO_3$ substrates. Obviously, for these applications we cannot use probe feeds as implied by Fig. 3.2. Instead, we use a monolithic microstrip feed network in which the feed lines are inset into the individual patches to achieve a match, as shown in Fig. 3.3. The relative phase differences between the patches is developed by appropriately adjusting the lengths of each line feeding a patch. As shown in the figure, we try to maintain as much symmetry in the feed network as possible.

To demonstrate the radiation characteristics of this design, we have plotted the principle plane (perpendicular to array feed line) spinning dipole pattern (Fig. 3.4) and a diagonal plane (45 deg. from array feed line) spinning dipole pattern (Fig. 3.5) for a 20 GHz Huang array on a 0.010 [in] $LaAlO_3$, as predicted by the expression in Sec. 3.2. For this example, the aspect ratio (W/L) of the patches is 1.5 and centers of the patches are separated by $0.5\lambda_o$. In the principal plane, the A.R. is excellent for large angles off broadside. Considering the four elements as a two element pair of linear elements (the pair side by side in the plane perpendicular to the principal plane) makes it clear why this performance is achieved. Each pair produces circular polarization since they are orthogonal in both space and phase. The shape of the radiation pattern is determined by the array factor in the principal plane due to the two pairs of elements. In the diagonal plane the array actually appears as a three element array with a 0^o-90^o-0^o phase configuration and a 1-2-1 amplitude distribution. The A.R. is therefore excellent at broadside, but suffers moderate degradation off broadside due to the difference in the array factors for the 0^o end elements and the two 90^o elements.

3.3.2: Gap-Coupled Array

A disadvantage of the 4-element Huang array is that every element must be feed with equal amplitude and with the appropriate phase to achieve good circular-polarization. If any one of the elements is excited weakly or not at all, the polarization of the array degrades significantly. To circumvent this potential problem, we have also investigated a more conventional circularly-polarized array. This array design, shown in Fig. 3.6, uses a microstrip feed network with gap-coupling to excite orthogonal modes on square microstrip patch elements with a phase differential of 90^o established by making the length of one of the orthogonal feed lines a quarter of a wavelength longer than the other. The gap size g is designed to provide a good match to the patch. In our layout, we have oriented the square patches at an angle of 45^o with respect to the feed in order to maintain as much symmetry in the orthogonal feed lines as possible. Since each element is circularly-polarized and the feed network to patch is the same, we expect that this array design will be less sensitive to non-uniform characteristics in the physical structure.

To demonstrate the radiation characteristics of this design, we have plotted the principle plane (plane perpendicular to array feed line) spinning dipole pattern (Fig. 3.7) and a diagonal plane (45 deg. from array feed line) spinning dipole pattern (Fig. 3.8) for a 20 GHz gap-coupled array on a 0.010 [in] $LaAlO_3$, as predicted by the expression in Sec. 3.2. For this example, the aspect ratio (W/L) of the patches is 1.0 and centers of the patches are separated by $0.5\lambda_o$. In the principal plane the A.R. is excellent at broadside and degrades slightly off broadside due to the difference in the E and H plane patterns of the square microstrip patch elements. The array factor for the four elements determines the shape of the overall radiation pattern. In the diagonal plane the array is in effect a three element array with a 1-2-1 amplitude distribution, as with the Huang array. For this array design though, each element produces circular polarization independently and therefore only the array factor, which produces a broad main lobe, degrades the A.R. off broadside by emphasizing the difference in the E and H plane patterns.

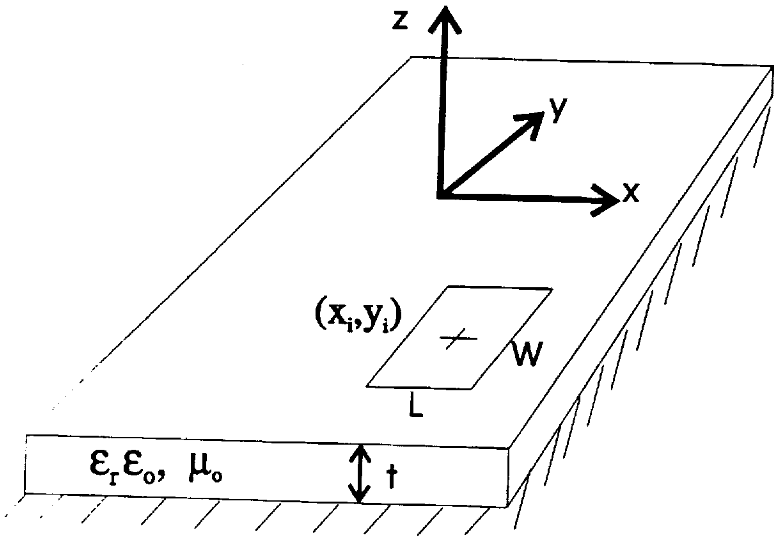

Figure 3.1: Geometry of a rectangular patch antenna centered at $(x_i,\ y_i)$.

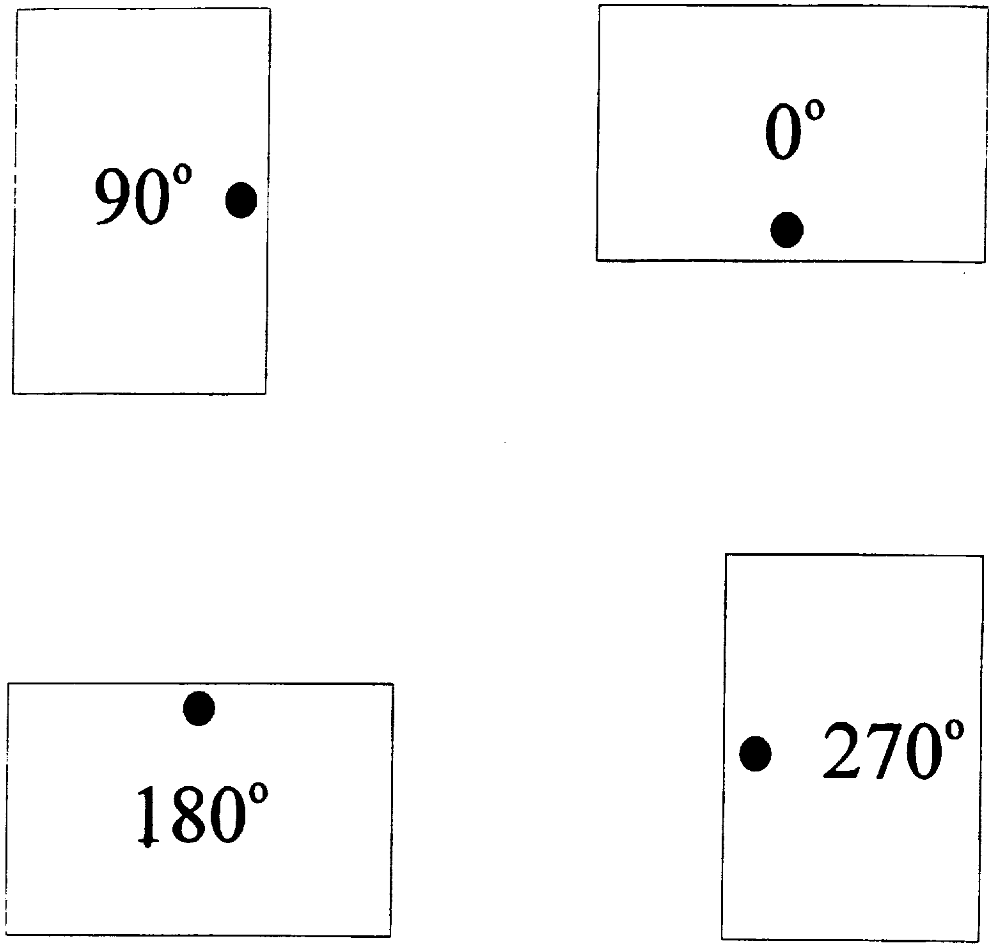

Figure 3.2: Orientation and phasing for a 4-element circularly polarized microstrip Huang array.

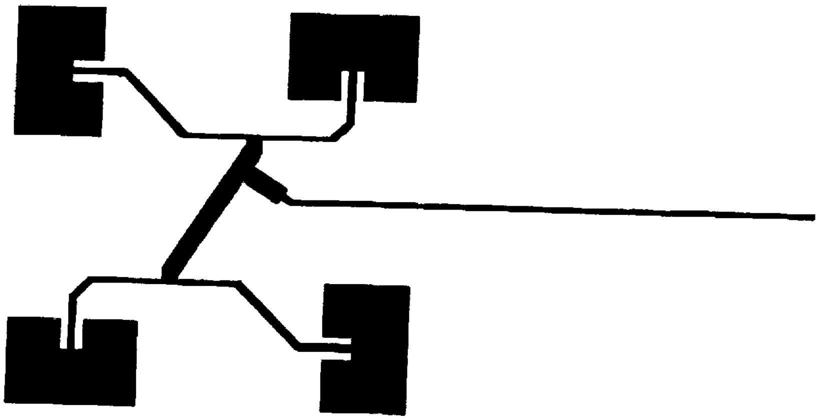

Figure 3.3: An example of a microstrip fed 4-element Huang array.

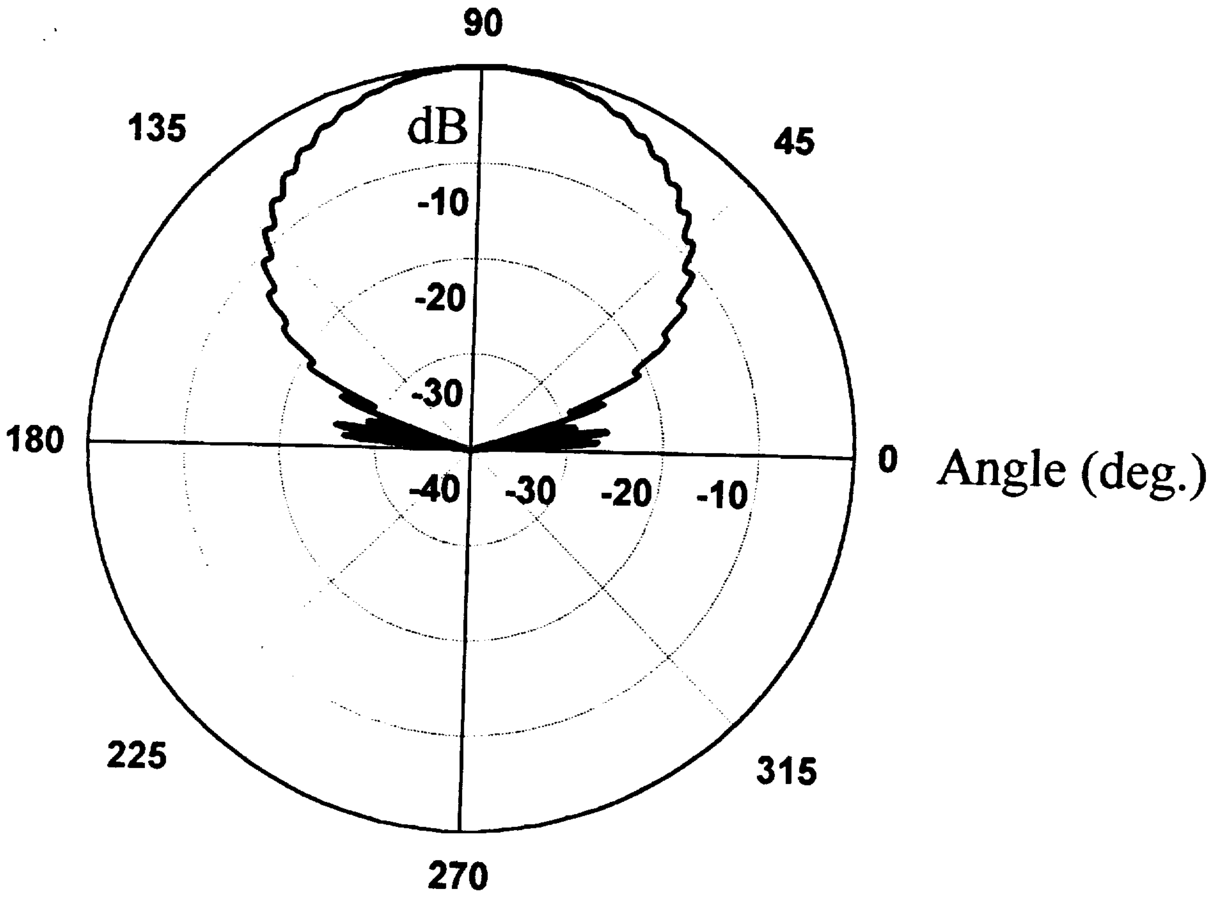

Figure 3.4: Principle plane (plane perpendicular to the input feed line) spinning dipole pattern for a 20 GHz Huang array on a $LaAlO_3$ substrate, with $0.5\lambda_o$ element spacing.

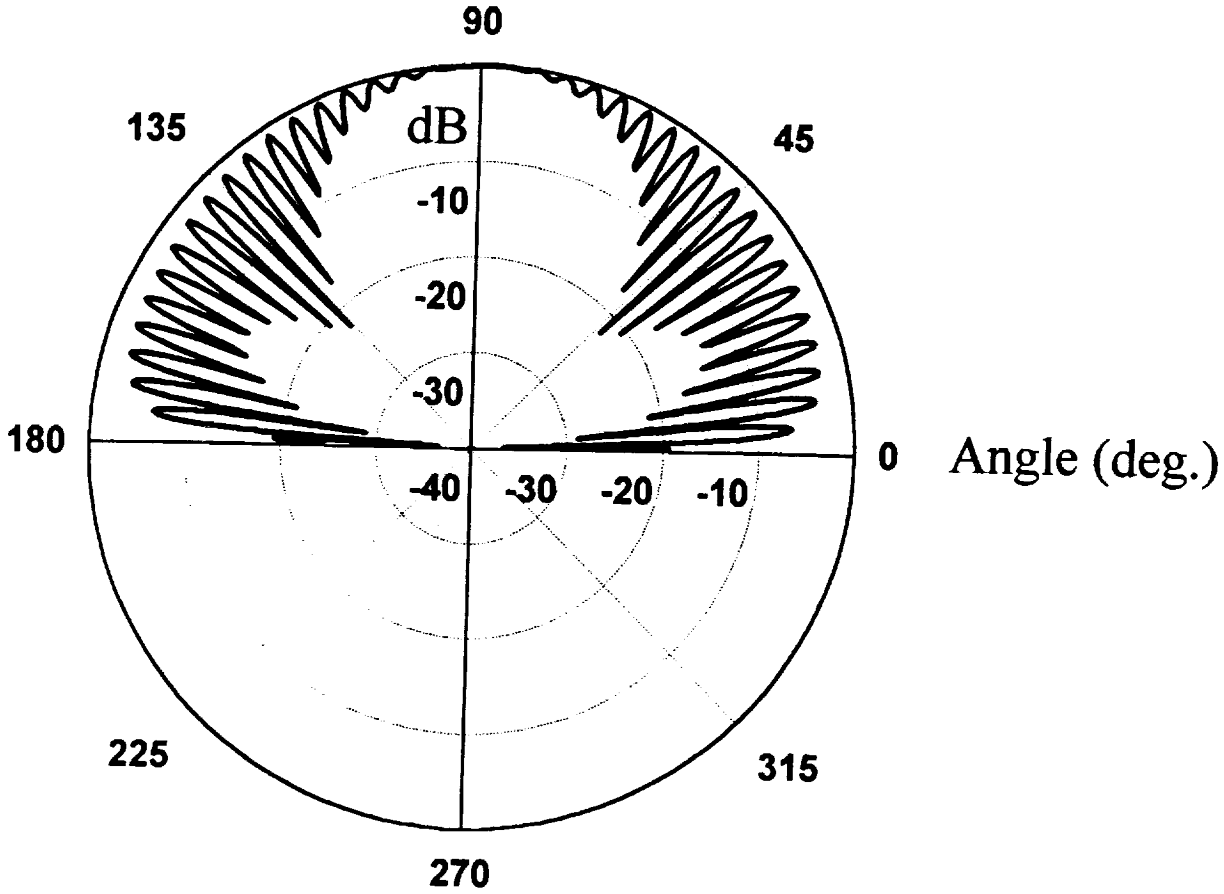

Figure 3.5: Diagonal plane (plane 45° with respect to the input feed line) spinning dipole pattern for a 20 GHz Huang array on a $LaAlO_3$ substrate, with $0.5\lambda_o$ element spacing.

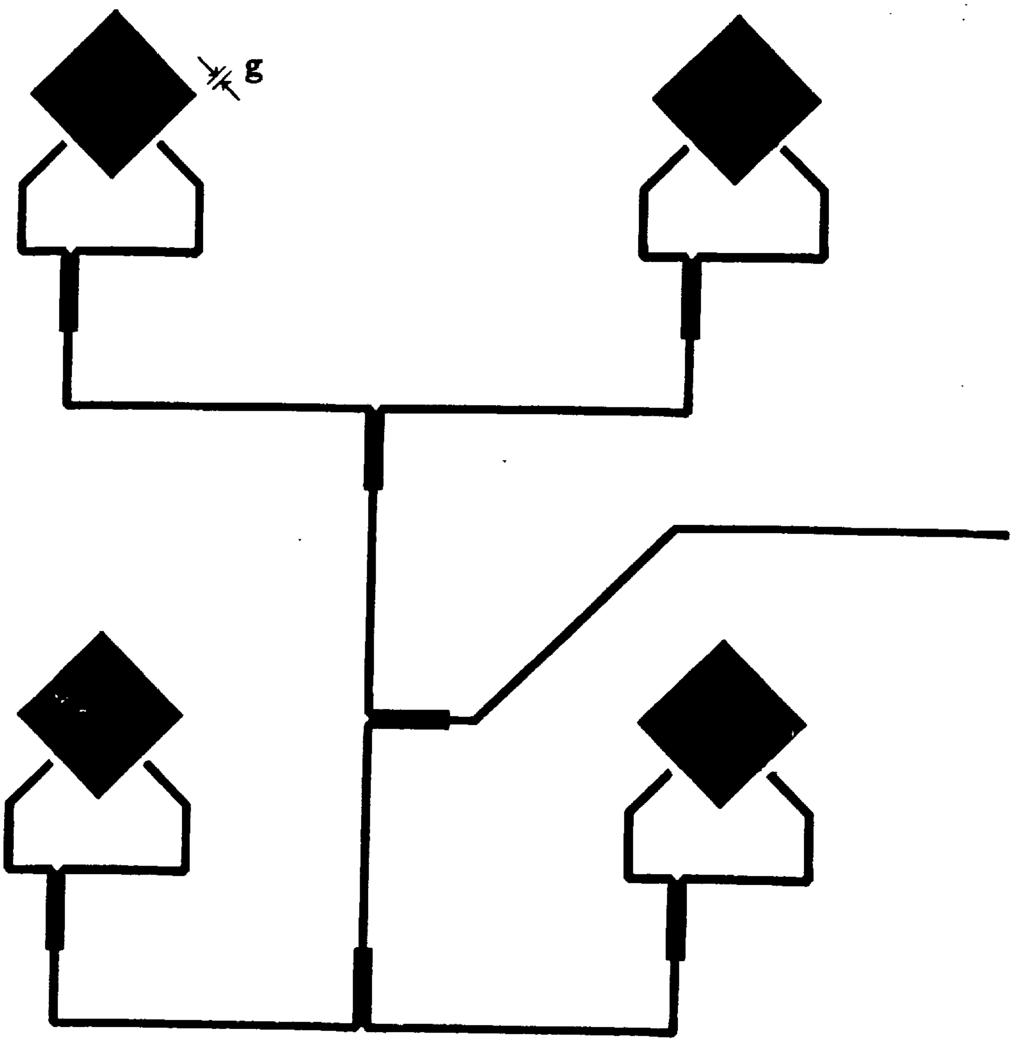

Figure 3.6: An example of a 4-element gap-coupled circularly polarized array.

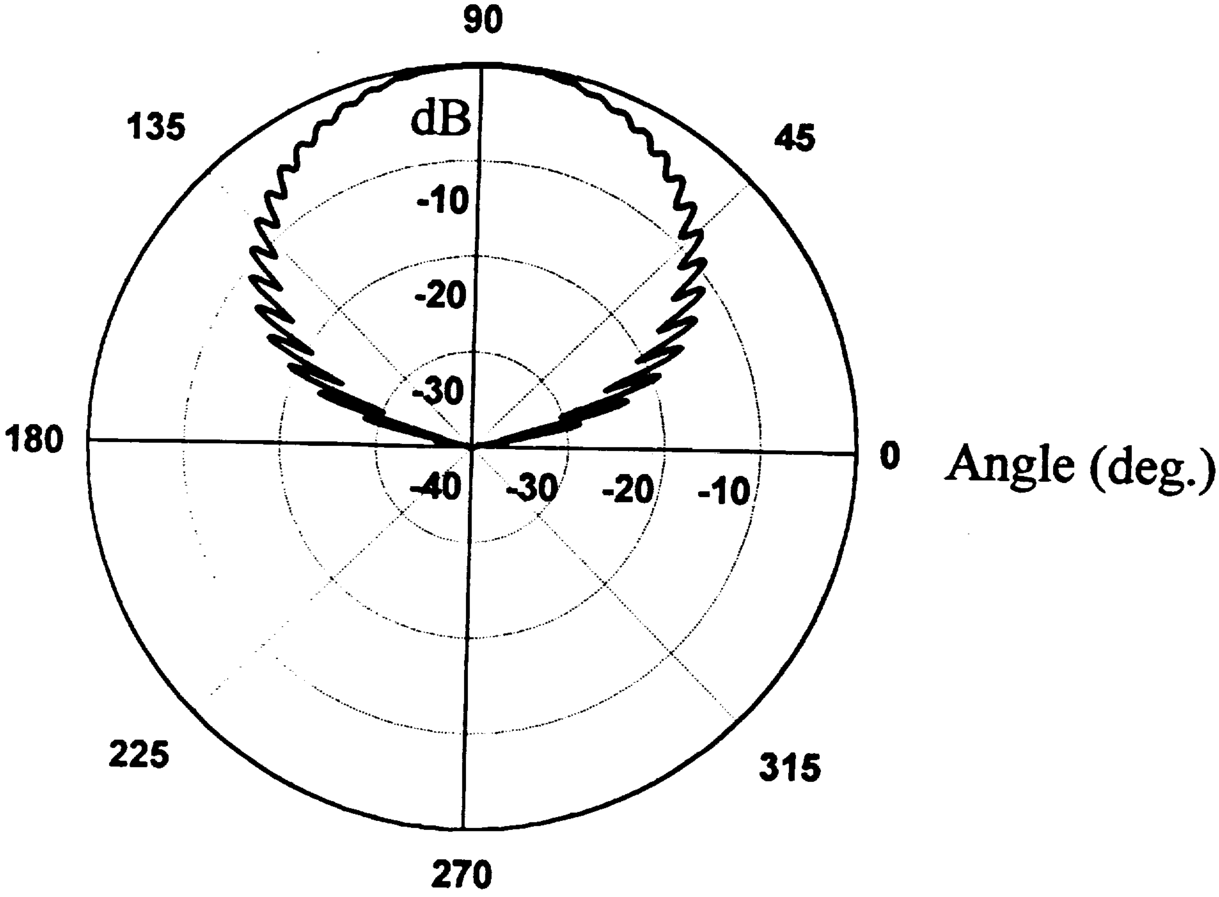

Figure 3.7: Principle plane (plane perpendicular to the input feed line) spinning dipole pattern for a 20 GHz gap-coupled array on a LaAlO3 substrate, with $0.5\lambda_o$ element spacing.

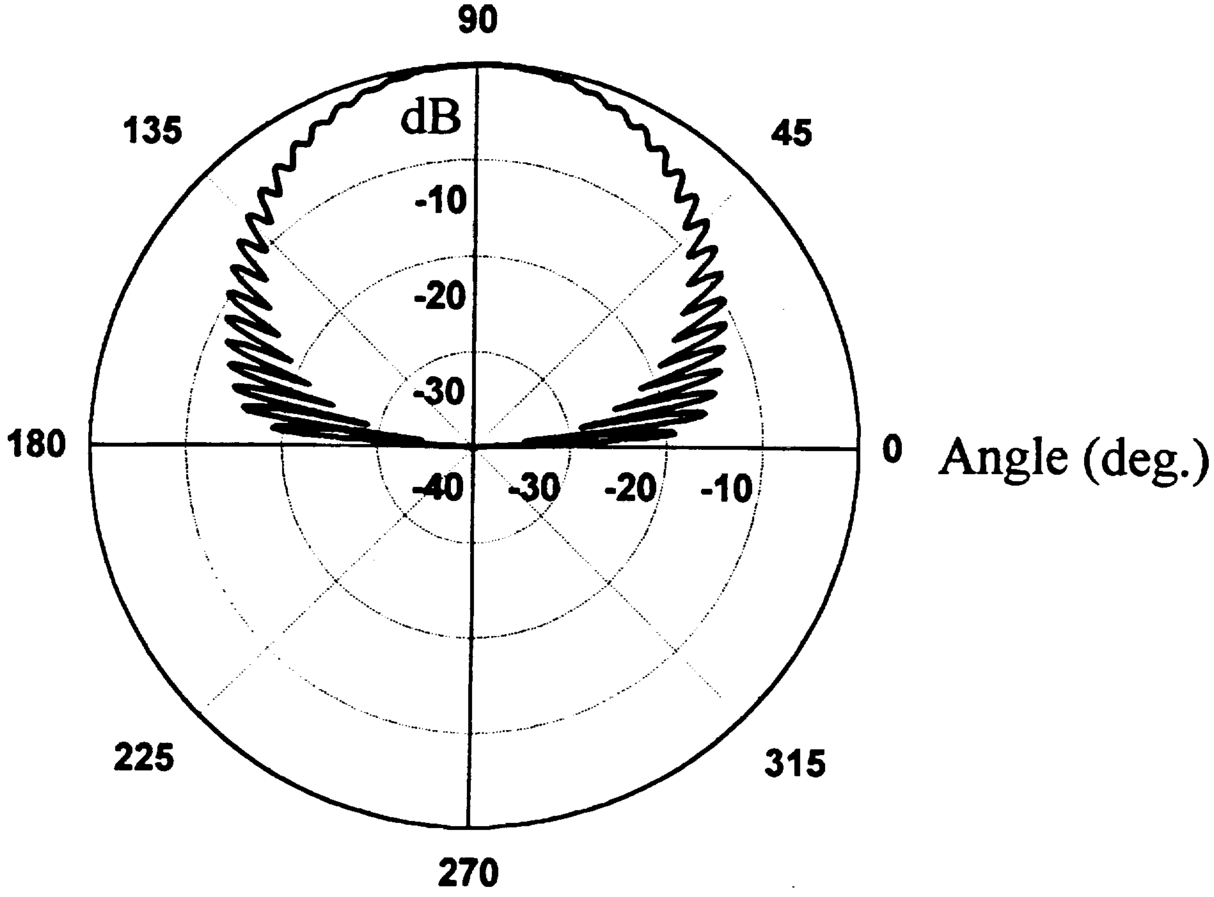

Figure 3.8: Diagonal plane (plane 45° with respect to the input feed line) spinning dipole pattern for a 20 GHz gap-coupled array on a $LaAlO_3$ substrate, with $0.5\lambda_o$ element spacing.

CHAPTER 4

Experimental Results

This chapter is devoted to the discussion of the experimental procedures and characterization of 4-element microstrip antenna arrays. We will discuss the experimental setups along with techniques used in the fabrication of the copper and superconducting antennas. The performance of the Huang array for initial 5 GHz test cases will be discussed. In addition, the results obtained for 20 GHz linear and circularly polarized gap-coupled copper elements and a copper circularly polarized gap-coupled array will be presented. The chapter concludes with a discussion of a superconducting circularly polarized 4-element gap-coupled microstrip array.

4.1: Experimental Setup and Procedures

In this section we will describe the experimental setup and procedures used in this investigation. We have divided this discussion into three parts. The first is a description of the test setups, in which we detail the mechanical and electrical components of the cryogenic platform for the superconductor measurements. Second, we discuss the general measurement procedures followed, and finally, we describe the materials and fabrication techniques used in the construction of the test antennas.

4.1.1: Test Setup

A schematic representation of the cryogenic system used in this investigation is shown in Fig. 4.1. This system is based around a 2-stage, closed-cycle helium cryogenic refrigerator. The second stage of the refrigerator is connected to the cold head in an evacuated chamber (cryostat) that is partial shielded by a radiation shield held at 77K. A copper cold head extension is used to support the antenna fixture and raise it to the top of the cryostat. The antenna fixture is constructed from brass, and is used to support the antenna-under-test (AUT) and the requisite feed lines (Fig. 4.2). In addition, this brass fixture supports a thin 8 [in] aluminum ground plane and a temperature sensing diode. All mechanical joints are sealed with indium foil to insure good thermal contacts. A hemispherical quartz dome is used as a window to the atmosphere for the fields of the antenna and also serves to seal the chamber. At 20 GHz, the electrical thickness of the dome is slightly over a wavelength.

A 0.047 [in] copper coaxial cable is connected from the coaxial feed-through connectors, located on one of the external ports of the cryostat, to the brass antenna fixture. In an attempt to improve the coax-to-microstrip transition, this cable is used to directly feed the microstrip line, instead of using a coaxial end-launch connector. For the circuits tested, a pressure contact was used between the coaxial center conductor and the microstrip trace.

4.1.2: Measurement Procedures

The pattern and gain measurements were made, using an HP8510B vector network analyzer, in a newly fabricated millimeter-wave antenna chamber (Fig. 4.3). The operating frequency range for this chamber is designed to be from approximately 15 GHz to 100 GHz. For most of the measurements the AUT is used as the receiving antenna and a standard gain horn as the transmitting antenna. The horn is supported and positioned by a pivot arm that is driven by a computer controlled stepper motor. The angular range of this arm is 180^o. To control the orientation (polarization) of the transmitting horn, we designed the dc-motor controlled fixture shown in Fig. 4.4. Using a coaxial rotary joint with this polarization fixture, we were able to orient the transmitting antenna in any transverse direction, or allow it to spin continuously for spinning dipole measurements.

One of the most meaningful measures of a superconducting antenna is a relative gain comparison between it and a normally conducting antenna of the same design. This is particularly true for array antennas since direct measurements of their efficiency is extremely difficult. Using Friis transmission formula one can readily determine that the relative gain of a superconducting antenna G_{sc} to a normally conducting antenna G_{nc} is

$$\frac{G_{sc}}{G_{nc}} = \frac{\frac{|S_{21}|^2_{sc}}{1-|S_{11}|^2_{sc}}}{\frac{|S_{21}|^2_{nc}}{1-|S_{11}|^2_{nc}}}. \tag{4.1}$$

In a cryogenic environment it is difficult to establish accurate and reliable calibrations for the measurement cables and connectors. However, for the gain measurements, it is particularly important to measure the magnitude of the reflection from the AUT as accurately as possible. Therefore, we perform a full 1-port open, short, and matched load calibration on the antenna side of the feed-through connector on the cryostat. This is the closest temperature stable connection to the AUT. In addition, a "thru" calibration is made of the temperature stable cables connected to the transmitting and receiving antennas to account for their insertion loss.

4.1.3: Materials and Fabrication

For the superconducting antenna arrays, we used 0.250 [μm] thick $YBa_2Cu_3O_x$ films deposited on 1"×1"×0.010" $LaAlO_3$ substrates using an *in-situ* scanned, laser ablation system. The films were fabricated by the Thin Film Applications Group in TcSUH (Texas Center for Superconductivity at the University of Houston). Before the YBCO deposition, a 2 [μm] thick layer of silver was evaporated on the back of the substrate to provide a ground plane for the antenna. This side of the substrate was then silver pasted to a 0.020 [in] thick sheet of nickel, thus providing a way to mount the substrate on the heater in the laser ablation system. For this investigation, we left the films on the nickel plate to give it a rugged support structure. We feel that this technique is potentially attractive for structures that must survive high levels of vibration or mechanical shock.

Using a Hunt HNR120 negative photo resist, we patterned the antenna using reactive ion-milling. This process uses an ultra pure argon feed gas with two acceleration grids in a large vacuum chamber. During this procedure the films are heat sinked to a large thermal mass to prevent over-heating. A 2 [μm] thick, 1 [mm] wide layer of silver was evaporated on the microstrip feed line to improve the contact between this line and the coax.

For comparison and prototype antenna structures, we used dc-sputtered copper films on $LaAlO_3$. Both sides of the substrate were coated with a 2 [μm] film of OFHC copper. The patterning of these copper films is essentially the same as described above, except a wet etch solution was used. The etchant used was a standard KI, I_2, H_2O gold etch. Standard copper etchants were found to etch these thin films too rapidly.

4.2: 4-Element Huang Array

We began our study of the 4-element Huang array by fabricating and testing prototypes of this structure on dielectric substrates of $\epsilon_r = 2.2$ and $\epsilon_r = 10.8$. The design frequency for these prototypes was 5 GHz. For the $\epsilon_r = 2.2$ material (thickness 0.0147"), we used the layout shown in Fig. 4.5. The microstrip feed network consists of a 50 Ω line impedance matched to the initial power divider by a 35 Ω quarter-wave transformer. Each 50 Ω output line from this power divider is connected to a power divider with 100 Ω output lines. These 100 Ω lines are inset into the rectangular microstrip patches ($W/L = 1.5$) to achieve a match. (The insets are not shown in this figure.) To obtain the desired 90^o phase differential between adjacent patches, the lengths of the lines feeding each patch as we rotate in a counter-clockwise direction from the upper right-hand patch is a quarter of a wavelength ($\lambda_g/4$) longer than its preceding neighbor.

In order to fit the feed network inside the array of patches and eliminate undesired coupling between the feed lines and the patch elements, we had to use $0.75\lambda_o$ spacings between the centers of the elements. As one would expect, this increases the side lobe level of the array. A theoretical spinning dipole pattern for this antenna, obtained using the expressions in Sec. 3.2, is shown in Fig. 4.6, and the experimental spinning dipole pattern is shown in Fig. 4.7. Both patterns are for the principal plane (the plane perpendicular with the input feed line). Note the good agreement between the theory and experiment. Both patterns demonstrate excellent CP performance at broadside. The circular polarization starts to degrade away from broadside. At angles beyond approximately 45^o from zenith both the axial ratio (A.R.) and the side lobes are large.

The side lobes in the previous patterns can be reduced by decreasing the spacing between the patches. This is readily accomplished by increasing the dielectric constant of the substrate. This reduces the size of the patch radiators, thereby providing more room between the elements for the feed network. Figure 4.8 shows the pattern for a 4-element Huang array on a 0.025 [in] thick, dielectric substrate with $\epsilon_r = 10.8$. The design is essentially the same as that on the $\epsilon_r = 2.2$ material, except the element spacing is $0.5\lambda_o$. The theoretical and experimental principal plane spinning dipole patterns are shown in Fig.s 4.9 and 4.10, respectively. Notice that the side lobe levels have decreased substantially, and the A.R. remains low for larger angles from broadside, as compared to the previous example.

Unfortunately, we found it extremely difficult to obtain this last experimental result. On the higher dielectric constant substrates, the antenna is very sensitive to mismatches, feed line-to-feed line and feed line-to-patch coupling. These problems perturb the delicate amplitude and phase relationships between the individual patches, causing significant performance degradation. As expected, the problems are exasperated on the $LaAlO_3$ substrates. In addition to the inherent problems demonstrated on the $\epsilon_r = 10.8$ substrates, the non-uniformities of $LaAlO_3$ make the design process nearly futile. We found that we were not able to scale any of our previous results. As a result, our attempts to build a 20 GHz 4-element Huang array on $LaAlO_3$ have been, to date, unsuccessful.

4.3: 4-Element Gap-Coupled Array

4.3.1: Copper Array

We were much more successful fabricating an operational 20 GHz, 4-element gap-coupled array. As we mentioned in Chapter 3, this array design is less sensitive to slight mismatches, line-to-line and line-to-patch coupling, and non-uniformities in the substrate. As a result, we were able to efficiently prototype the design on $LaAlO_3$ at 20 GHz using copper elements with copper ground planes. The first step in the design process was to determine the appropriate gap dimension to obtain a low VSWR match between the patch and a 50 Ω feed. Using the linearly polarized microstrip element shown in Figure 4.11, we varied the gap dimension until a good match was obtained. The resonant dimension (physical dimension) of the patch L was determined from the following empirical expression:

$$L = \frac{\lambda_o}{2\sqrt{\epsilon_r}} - \frac{t}{2}, \tag{4.2}$$

where t is the thickness of the substrate. For a square 20 GHz patch ($W = L$), assuming a 0.010 [in] thick $LaAlO_3$ substrate with a dielectric constant of 23, L is equal to 1.437 [mm]. A plot of the magnitude of the reflection coefficient for this linear element with a 15 [μm] gap is shown in Fig. 4.12. Note that the reflection coefficient is approximately -25 dB at 19.55 GHz. A shift of the resonant frequency away from the 20 GHz design occurred for each structure tested; however, the shift was not consistent enough at the time of these measurements to dictate the change required in the design assumptions.

Next, using 15 [μm] gaps, a single gap-coupled circularly polarized copper element was fabricated. This antenna is shown in Fig. 4.13. The 50 [Ω] input line is matched to the 50 [Ω] feed lines out of the power divider using a 35 [Ω] quarter wave transformer. The lengths of the individual feed lines differ by a quarter wavelength in order that the two orthogonal modes of the patch are excited with a 90^o phase difference. The reflection coefficient corresponding to this element is presented in Fig. 4.14. Notice at 19.545 GHz, the reflection coefficient has a sharp null. At this frequency there is an effective match; however, the sharpness probably indicates that the resonances of the structure (patch resonances and quarter-wave transformer resonance) are at slightly different frequencies.

Figure 4.15 shows the theoretical spinning dipole pattern for this element, and Fig. 4.16 shows the corresponding experimental pattern. These patterns are taken in the plane indicated in Fig. 4.13. Comparing these responses, we immediately observe the ripples in the experimental patterns. These features are primarily due to the scattering of the patch excited surface-wave fields at the edges of the substrate, and the fields diffracted by the edge of the circular ground plane. These scattered and diffracted fields interfere with the primary fields radiated by the antenna, producing the periodic scalloping observed in Fig. 4.16. In addition to perturbing the shape of the pattern, these undesired fields also tend to degrade the axial ratio. Yet, in spite of these perturbing factors the A.R. near broadside is reasonable. The performance of this circularly polarized element was encouraging.

Next, these single CP elements were combined as shown in Fig. 4.17 to form a 2×2 gap-coupled circularly polarized microstrip array. The microstrip feed network consists of 50 [Ω] lines, with 35 [Ω] quarter-wave transformers at the T-junctions for matching purposes. For this array the spacing between the element centers is $0.5\lambda_o$.

The magnitude of the reflection coefficient for this array is shown in Fig. 4.18. This response is similar in many respects to that for the single CP element (Fig. 4.14). The primary differences are a small shift in the match frequency, and the minimum return is only approximately -23 dB. A theoretical spinning dipole pattern for this antenna in the plane that lies perpendicular to the input feed line (principle plane) is presented in Fig. 4.19. The corresponding experimental pattern is shown in Fig. 4.20. In general, there is relatively good agreement between the two patterns. The primary differences are the scalloping due to surface-wave scattering and edge diffraction, and the A.R. for the experimental array is a bit high at broadside. We feel that the discrepancies between the theoretical and experimental axial ratios are due primarily to the differences in the measured resonant frequency (19.565 GHz) and the 20 GHz design frequency. This error will affect the phasing between the orthogonal feeds of the individual patches, causing an increase in the A.R. In addition to these patterns we also have theoretical and experimental spinning dipole patterns in the plane at a 45^o angle with respect to the input feed line (diagonal plane). These patterns are presented in Fig.s 4.21 and 4.22, respectively. Basically, the behavior is the same as that in the perpendicular plane, except the overall patterns are broader.

The quartz dome used to seal the chamber is not optimal as a 20 GHz radome because it is relatively thick and this thickness varies, particularly near zenith. When placed over the copper antenna, the quartz dome introduced a moderate amount of pattern distortion. However, for making relative gain measurements between normally conducting and superconducting antennas of the same design, the pattern distortion is unimportant since the effects are the same for each structure.

After the satisfactory operation of the normally conducting copper array was verified, we attempted to measure its performance at cryogenic temperatures. Unfortunately, the thin copper microstrip lines on this structure lifted off easily and could not handle the mechanical stresses of multiple measurements and cooling.

4.3.2: $YBa_2Cu_3O_x$ Array

The final measurements were made for a $YBa_2Cu_3O_x$ version of the 2×2 copper array described in the previous section (Fig. 4.17). This antenna was fabricated as described in Sec. 4.1.3. The etched YBCO array had remarkably few defects. Those of importance were that the gaps between the feed lines and the patches were slightly over etched, approximately 18-20 [μm] compared to the 15 [μm] design value, and the thickness of one of the microstrip lines at the edge of a patch was thinned during the etching of the circuit. Still, for all temperatures below the transition temperature of the YBCO array (which was measured to be approximately 85K) the return loss was very small, below 25-30 dB. In addition, the spinning dipole pattern at resonance was essentially the same as that for the copper array covered by the quartz dome. The primary difference was that the axial ratio for the YBCO array was approximately 4-5 dB larger than that of the copper array. This increased A.R. was probably a result of the over etched feed gaps and thinned feed line, both of which could result in an amplitude and phase imbalance between the orthogonal polarizations of the antenna.

A plot of the measured gain of the $YBa_2Cu_3O_x$ microstrip array relative to the room temperature ($300K$) copper array is shown in Fig. 4.23. This result shows a sharp transition at approximately $85K$, with the relative gain increasing above 0 dB for temperatures below $82K$. The relative gain increases with decreasing temperature, reaching a value of greater than 3.4 dB at $30K$. In addition, to the measured gain, we have provided a point which shows the theoretically predicted value of 1.67 dB at $77K$. This value was obtained using the analysis detailed in Chapter 2. The parameters for these models are those specified in previous sections, except the assumed value for the conductivity of silver at $77K$ was 42.5×10^7 [S/m]. As observed in Fig. 4.23, the theoretical and measured values of the relative gain of the YBCO antenna at $77K$ to the $300K$ copper antenna are comparable.

In the range of temperature between transition and approximately $72K$, the value of the resonant frequency was difficult to determine accurately. In this temperature range the resonant frequency is changing substantially due to the rapidly changing effective penetration depth of the superconductor. A plot of the measured resonant frequency versus temperature is shown in Fig. 4.24. As a result of the uncertainty in the resonant frequency, relative gains that we measured were slightly unstable. However, for temperatures below approximately $72K$ the measure resonance was easily identifiable and the corresponding gain measurements were steady.

These results do not represent the conclusion of this investigation. We are currently in the process of improving the gap-coupled design with the aim of decreasing its axial ratio. We believe that the primary reason for the non-zero A.R. at broadside is that the dielectric constant of the $LaAlO_3$ substrate does not equal 23, the value assumed in this design. From our measurements, we believe that for this substrate vendor the dielectric constant is closer to 24. This difference in ϵ_r would account for the difference between the measured and design resonant frequency of the patch antennas. After the design of the 4-element array has been optimized, we plan to fabricate and test a 16-element gap-coupled array.

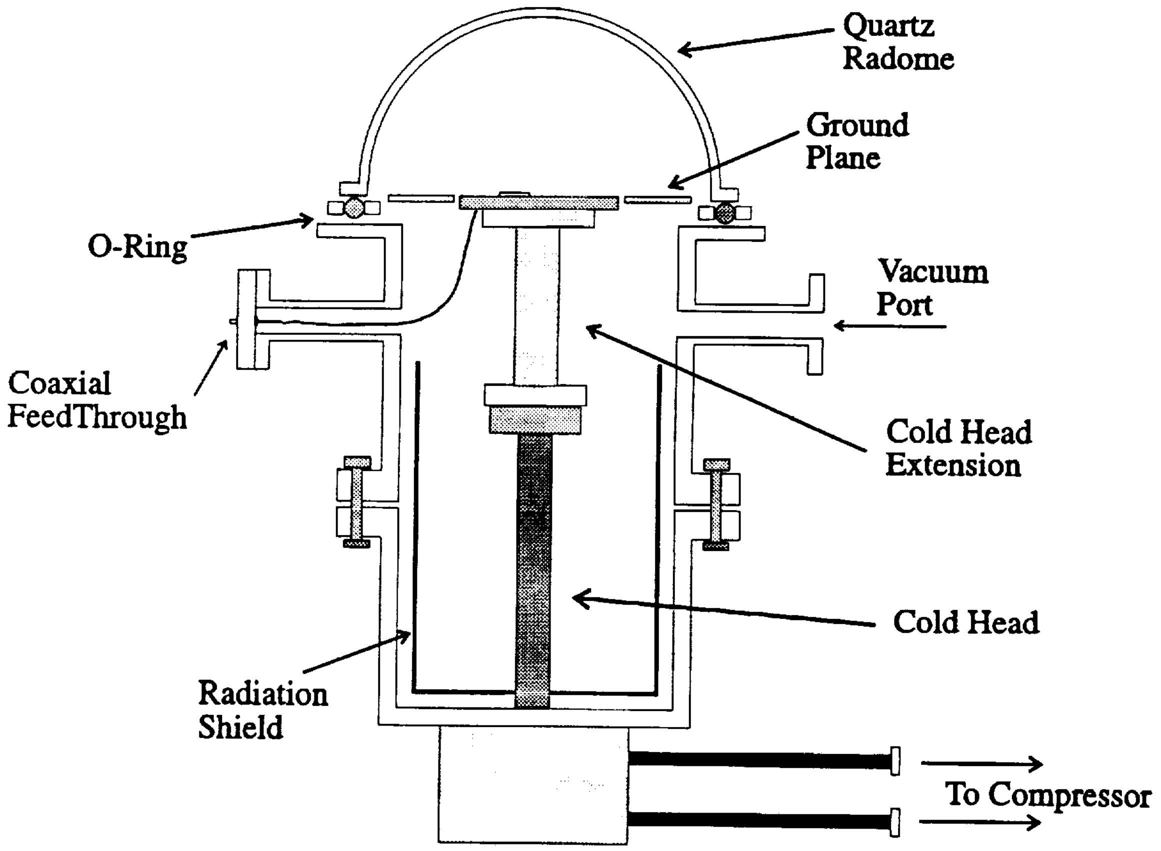

Figure 4.1: Schematic representation of the test setup used for cryogenic antenna measurements.

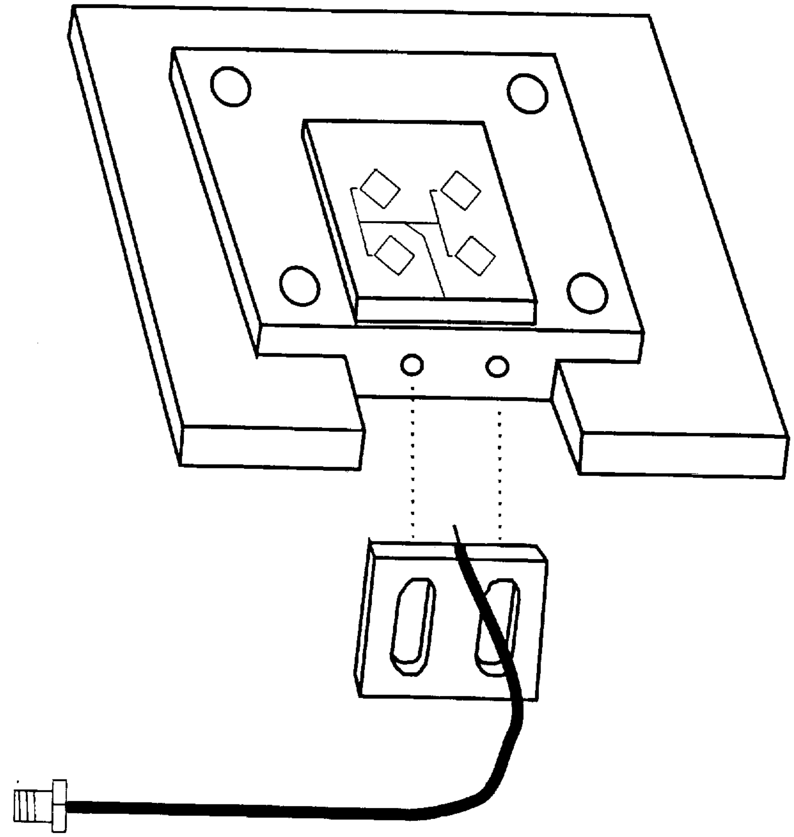

Figure 4.2: Antenna mounting fixture.

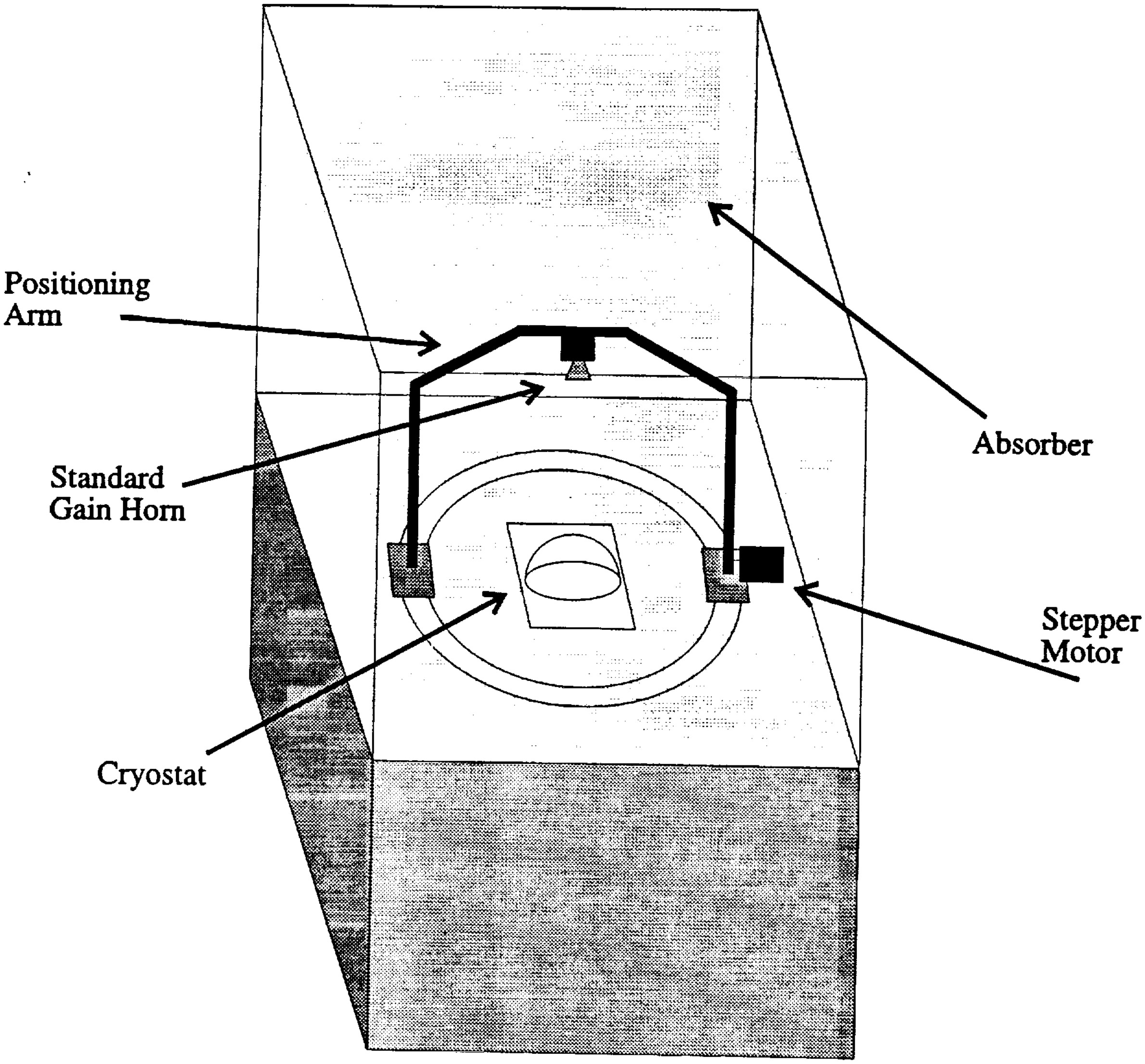

Figure 4.3: Millimeter-wave antenna measurement chamber.

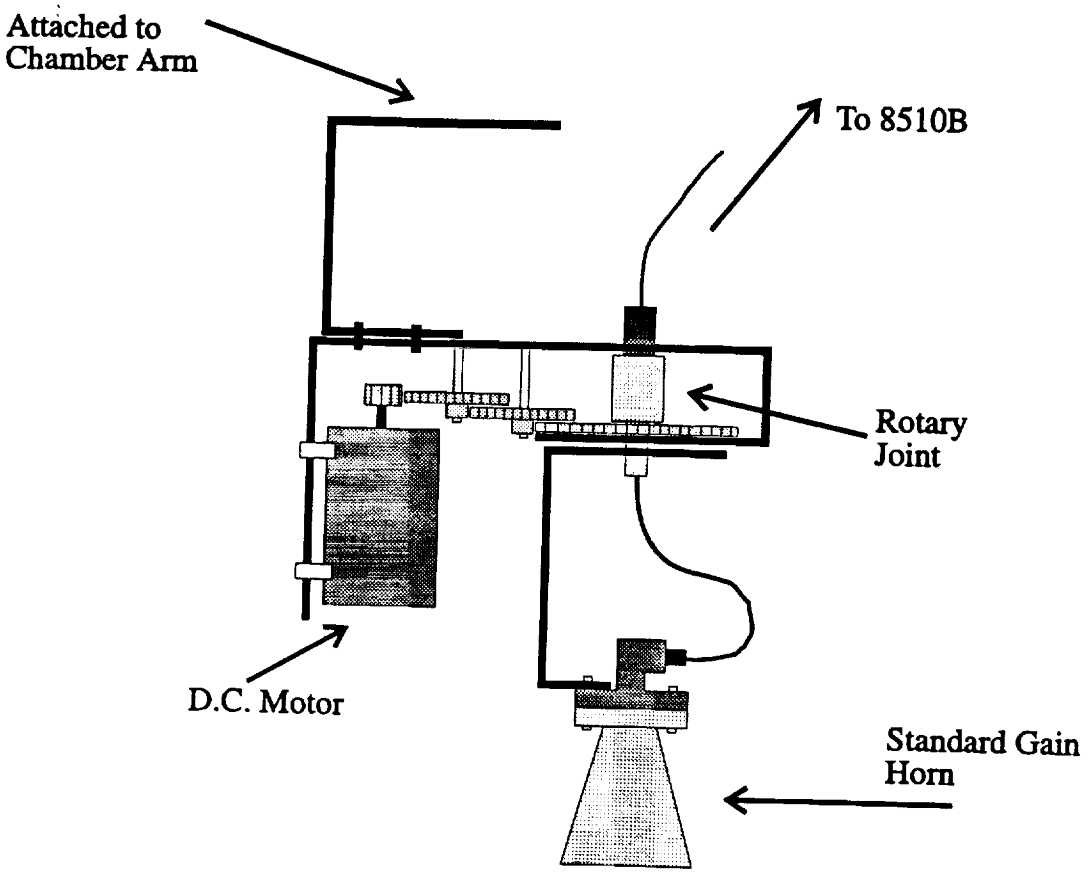

Figure 4.4: Motor controlled polarization unit.

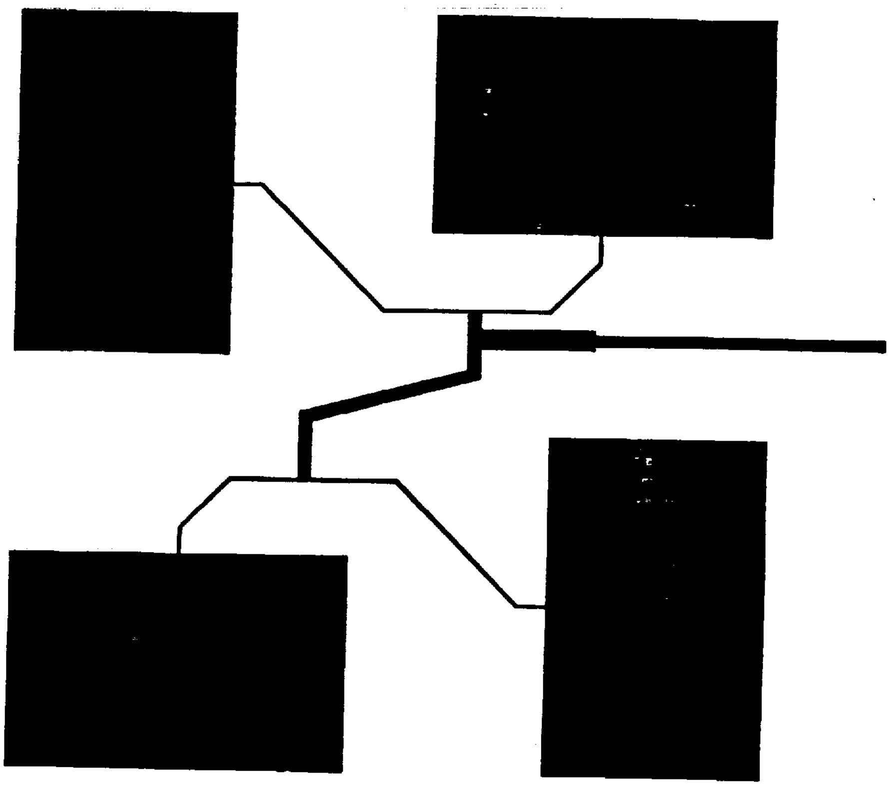

Figure 4.5: 5 GHz, 4-element Huang array on duroid substrate ($\epsilon_r = 2.2$, $t = 0.0147$ [in]), with a $0.75\lambda_o$ element spacing.

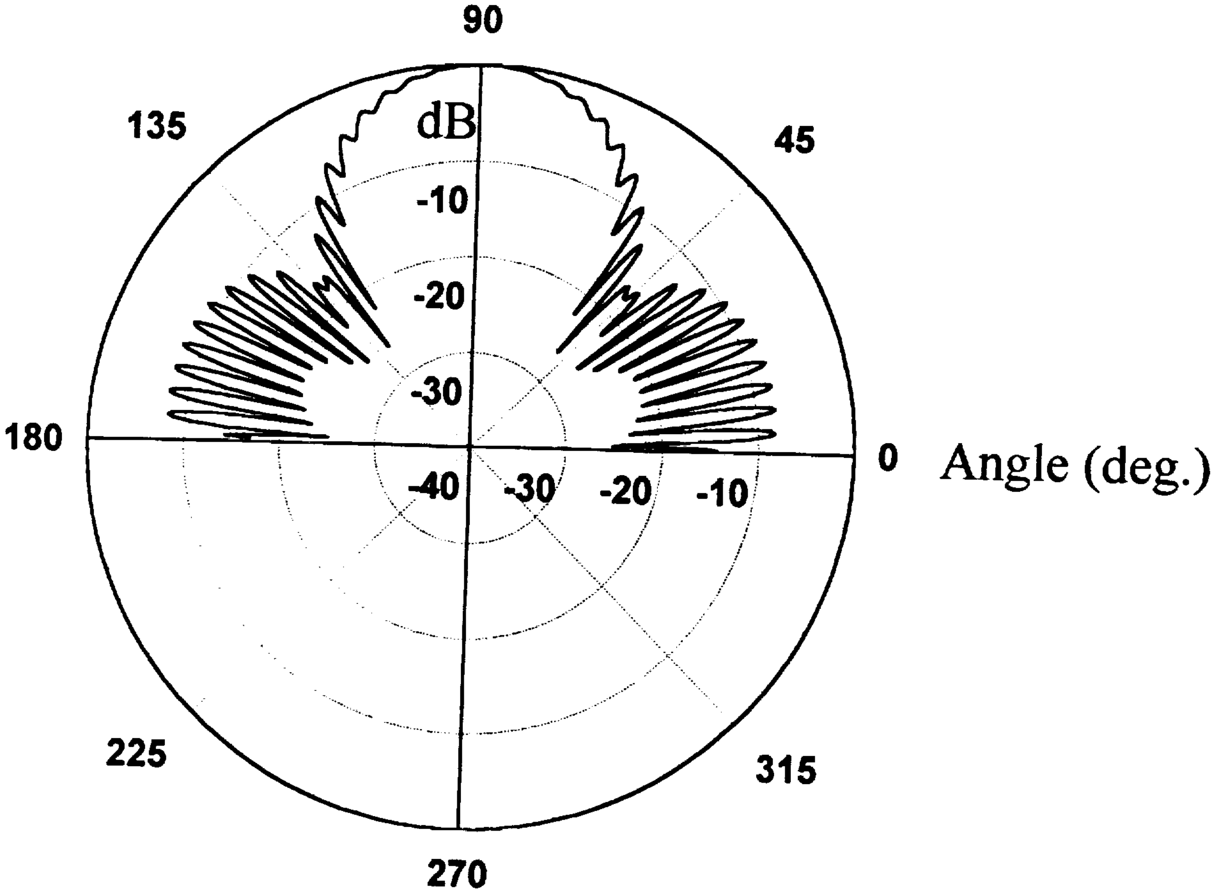

Figure 4.6: Theoretical principle plane spinning dipole pattern for the 4-element Huang array in Fig. 4.5.

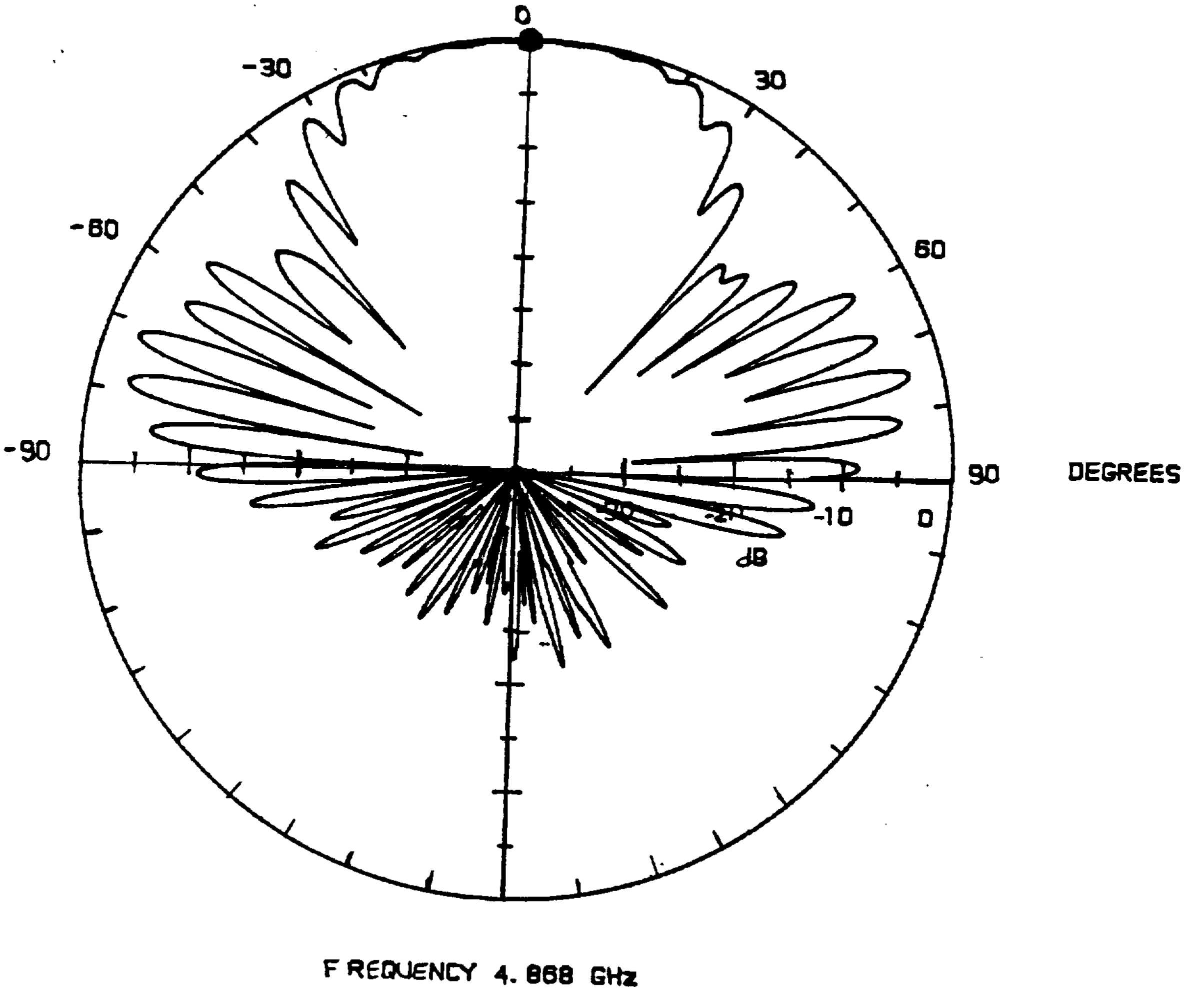

Figure 4.7: Measured principle plane spinning dipole pattern for the 4-element Huang array in Fig. 4.5.

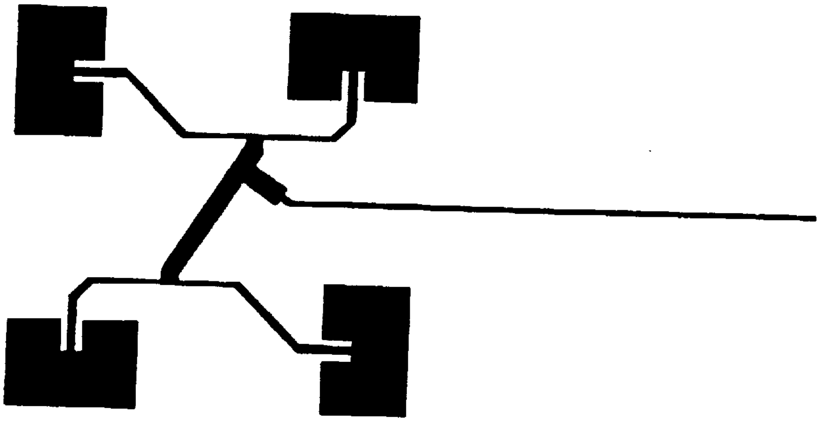

Figure 4.8: 5 GHz, 4-element Huang array on duroid substrate (ϵ_r = 10.8, t = 0.025 [in]), with a $0.5\lambda_o$ element spacing.

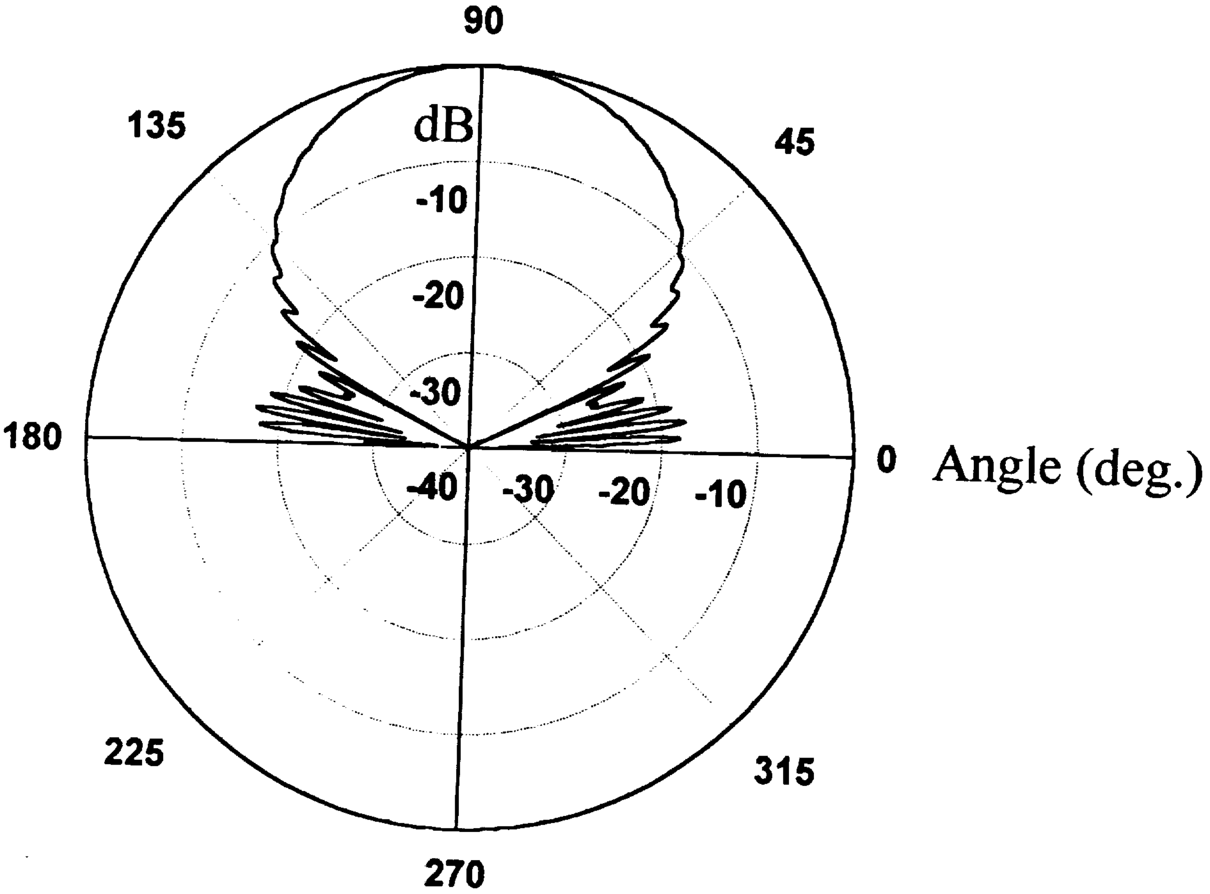

Figure 4.9: Theoretical principle plane spinning dipole pattern for the 4-element Huang array in Fig. 4.8.

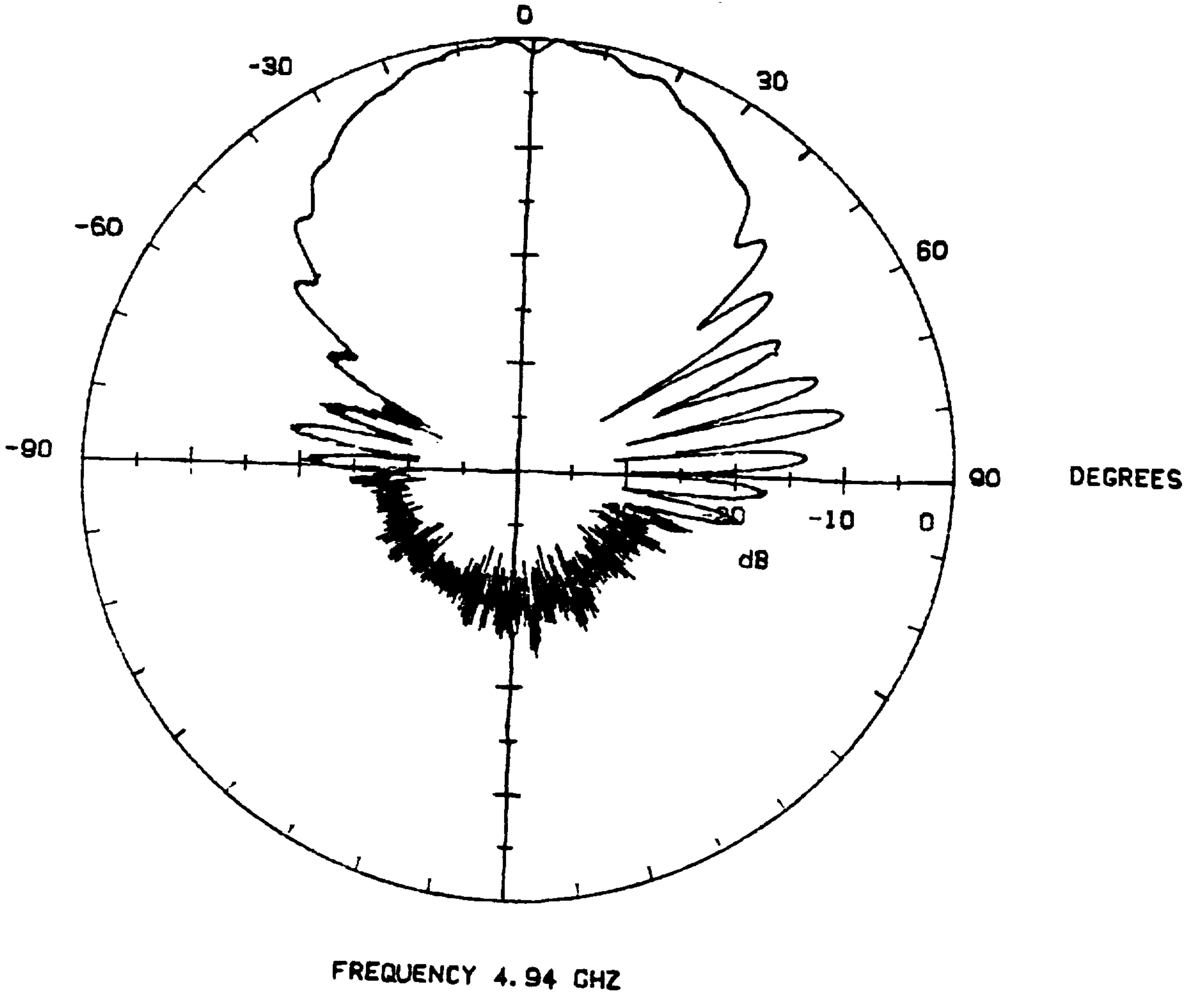

Figure 4.10: Measured principle plane spinning dipole pattern for the 4-element Huang array in Fig. 4.8.

Figure 4.11: 20 GHz, linearly polarized gap-coupled patch antenna ($W/L = 1$) on 0.010 [in] $LaAlO_3$.

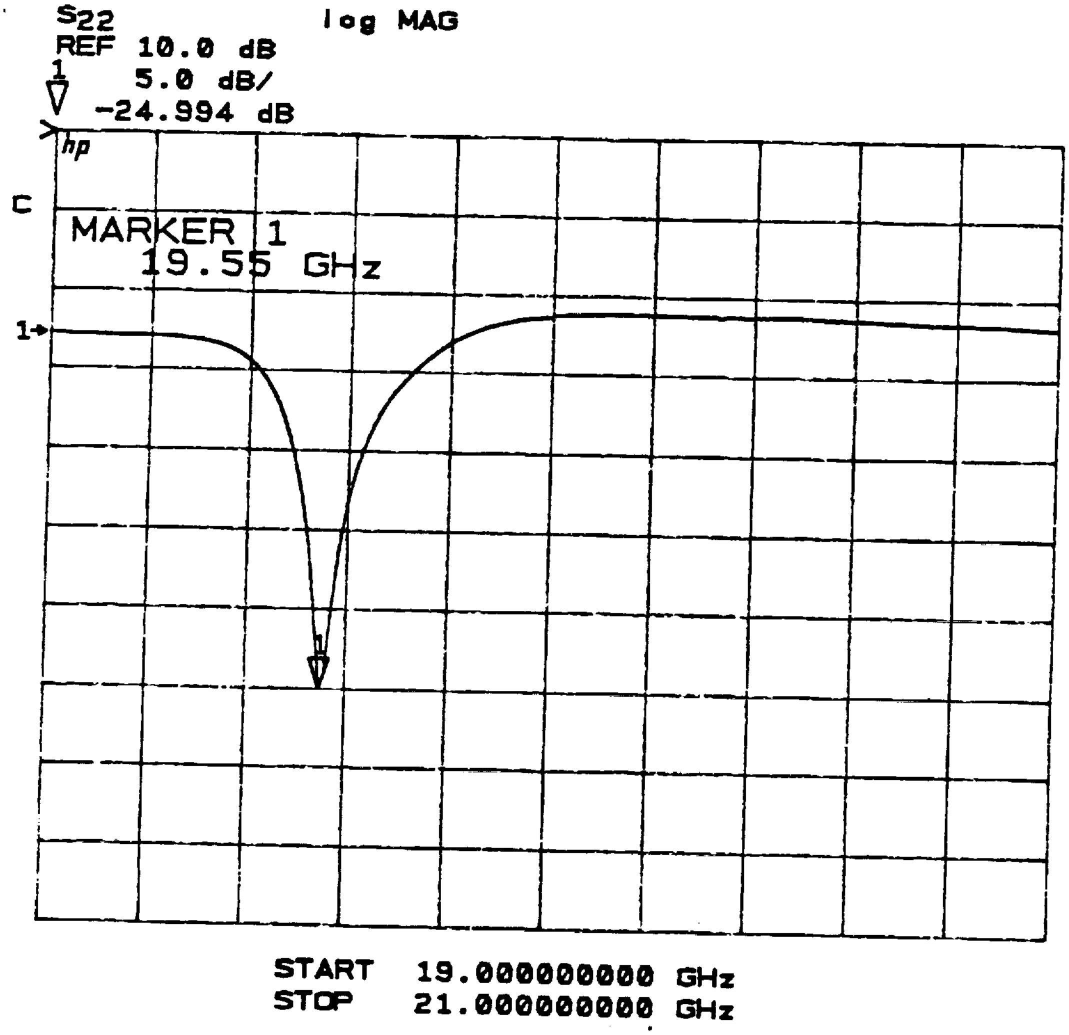

Figure 4.12: Measured magnitude of the reflection coefficient for the linearly polarized gap-coupled patch antenna in Fig. 4.11.

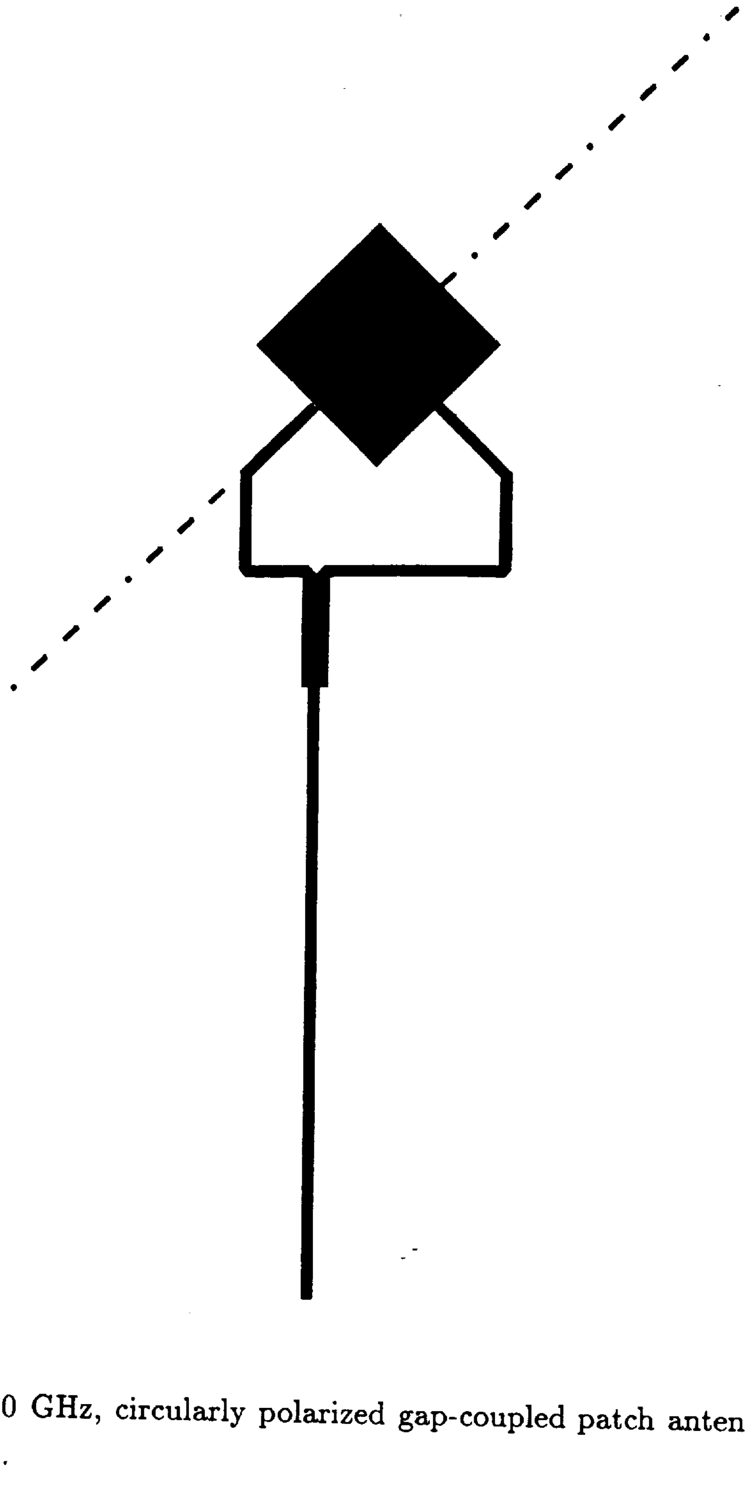

Figure 4.13: 20 GHz, circularly polarized gap-coupled patch antenna ($W/L = 1$) on 0.010 [in] $LaAlO_3$.

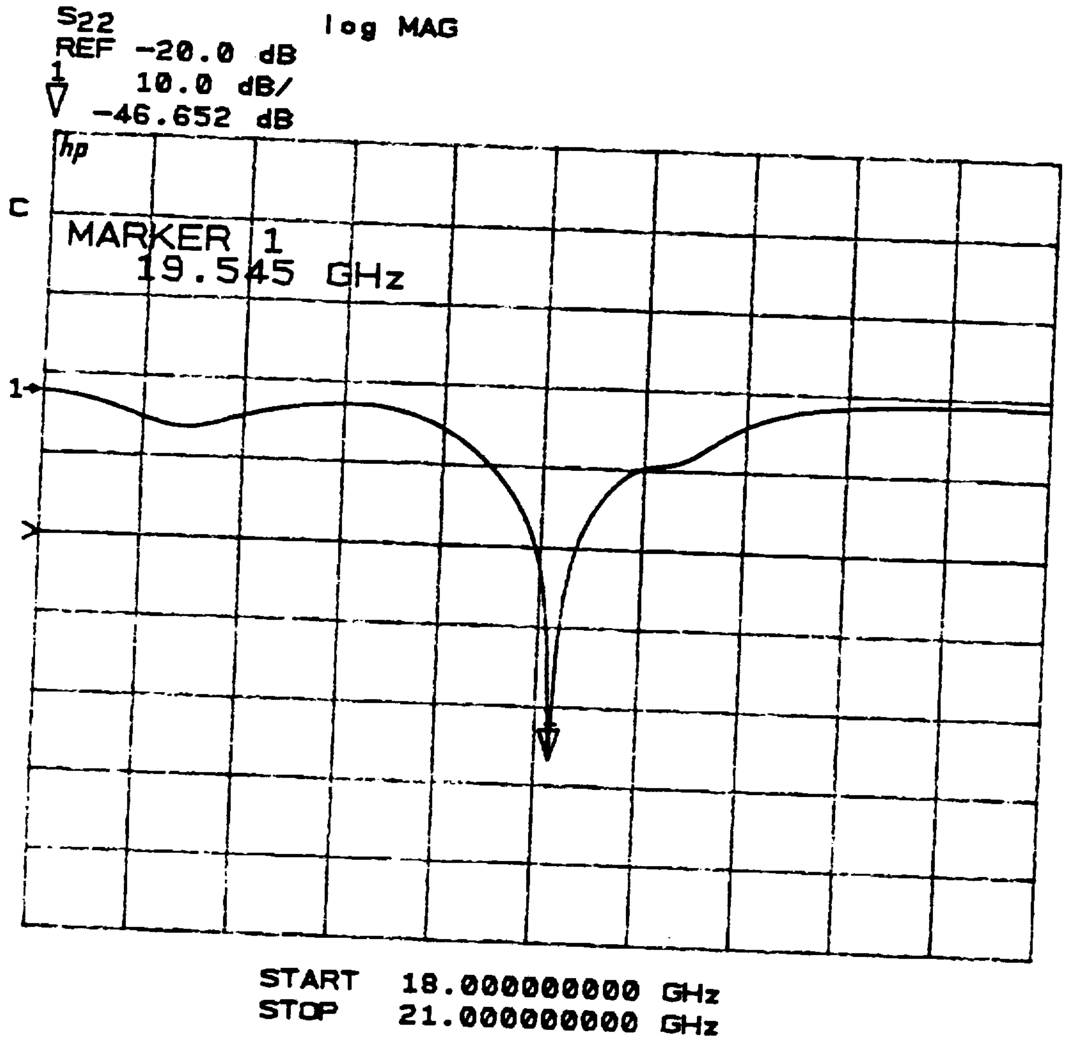

Figure 4.14: Measured magnitude of the reflection coefficient for the circularly polarized gap-coupled patch antenna in Fig. 4.13.

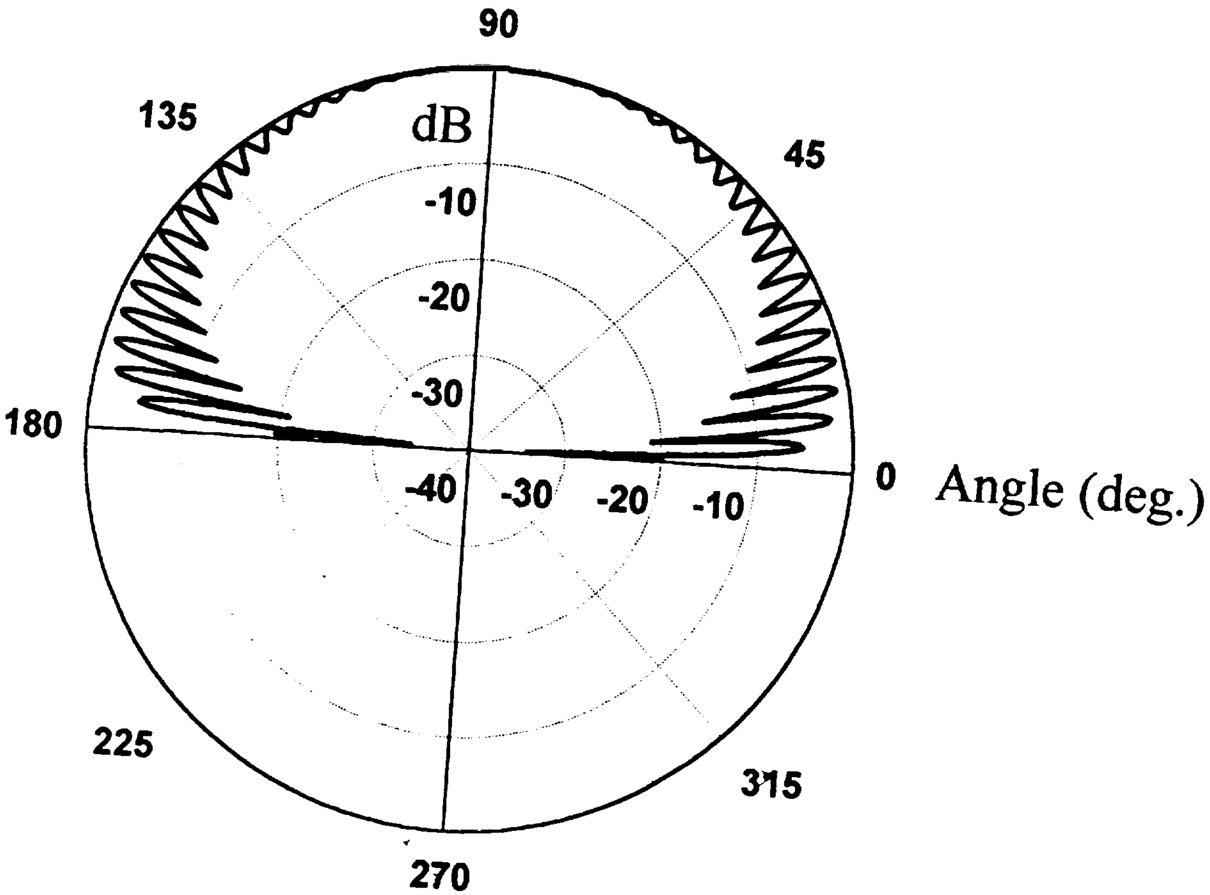

Figure 4.15: Theoretical principle plane spinning dipole pattern for the circularly polarized gap-coupled patch antenna in Fig. 4.13.

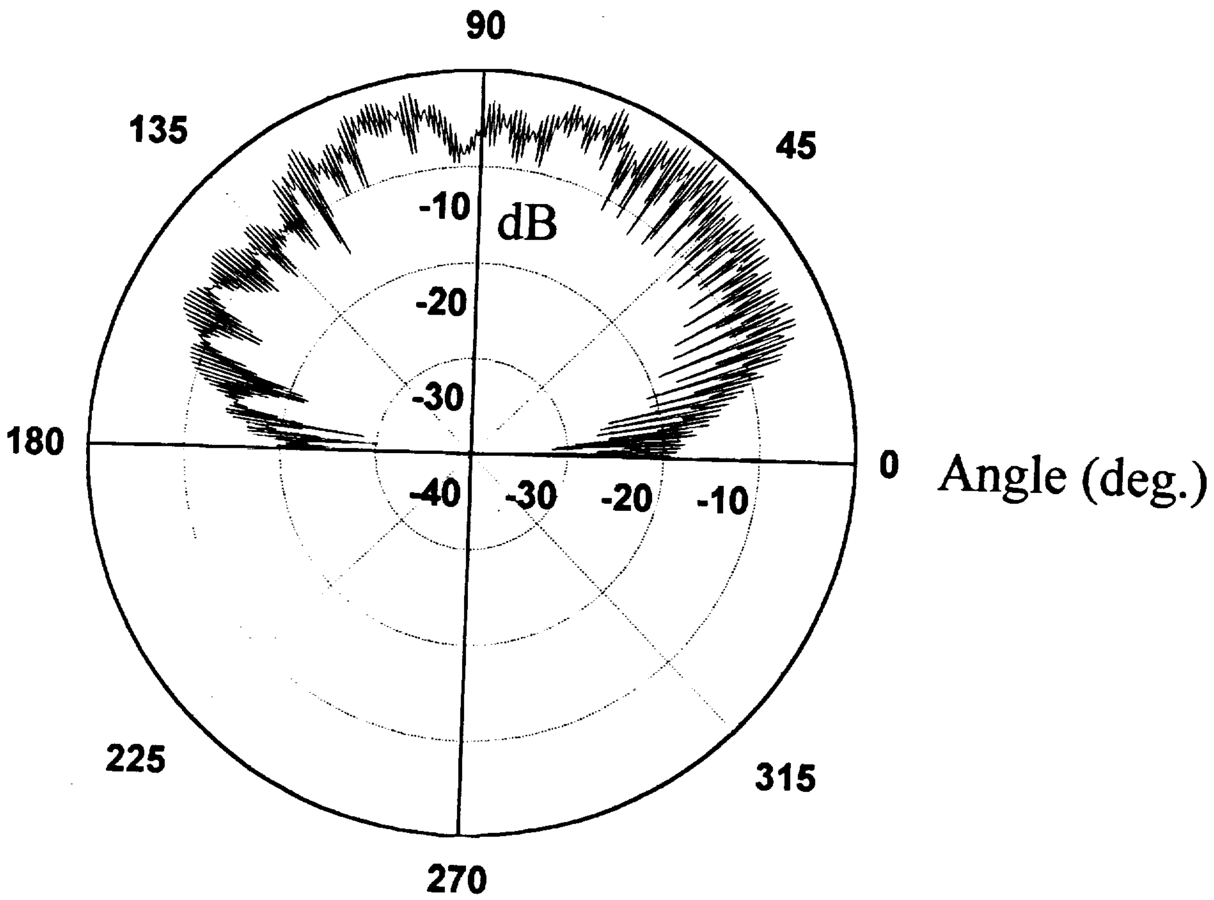

Figure 4.16: Measured principle plane spinning dipole pattern for the circularly polarized gap-coupled patch antenna in Fig. 4.13.

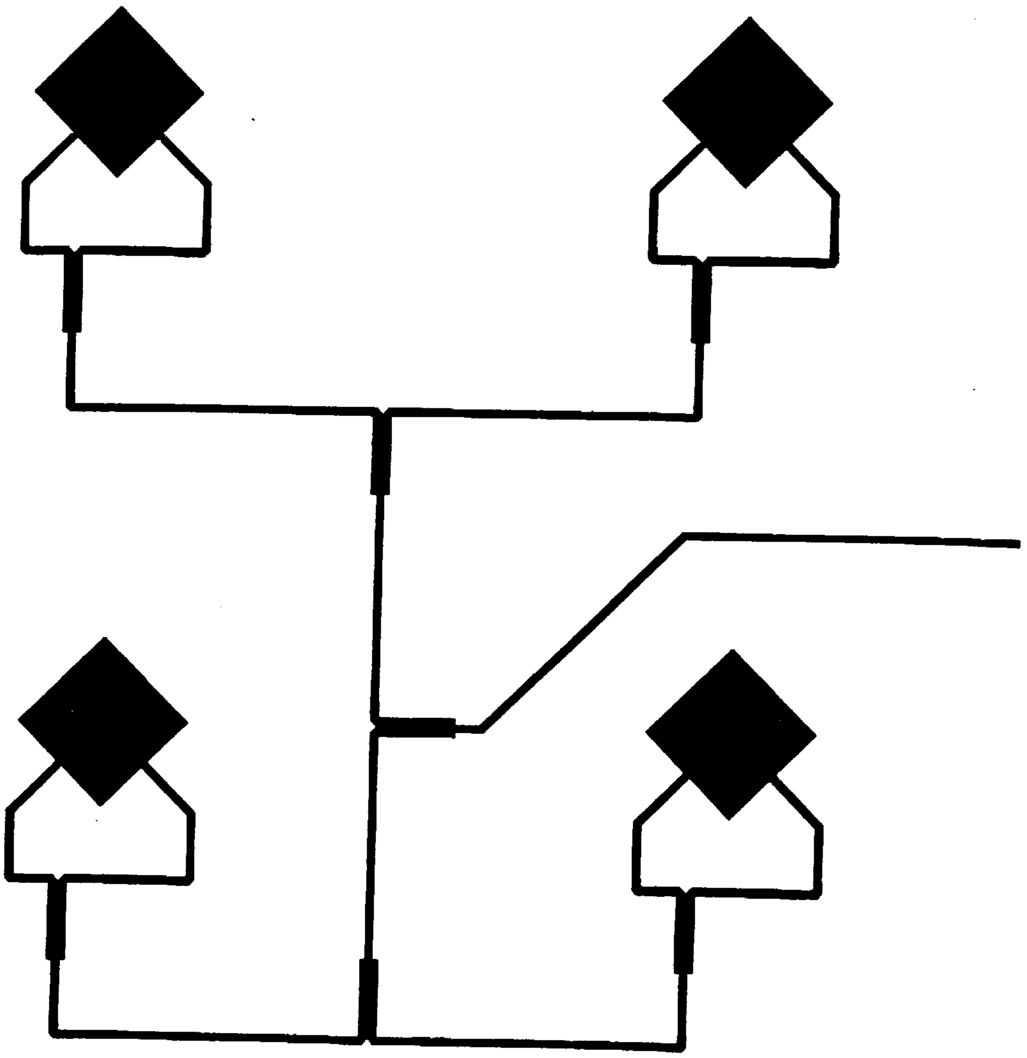

Figure 4.17: 20 GHz, circularly polarized 4-element gap-coupled patch antenna array ($W/L = 1$) on 0.010 [in] $LaAlO_3$.

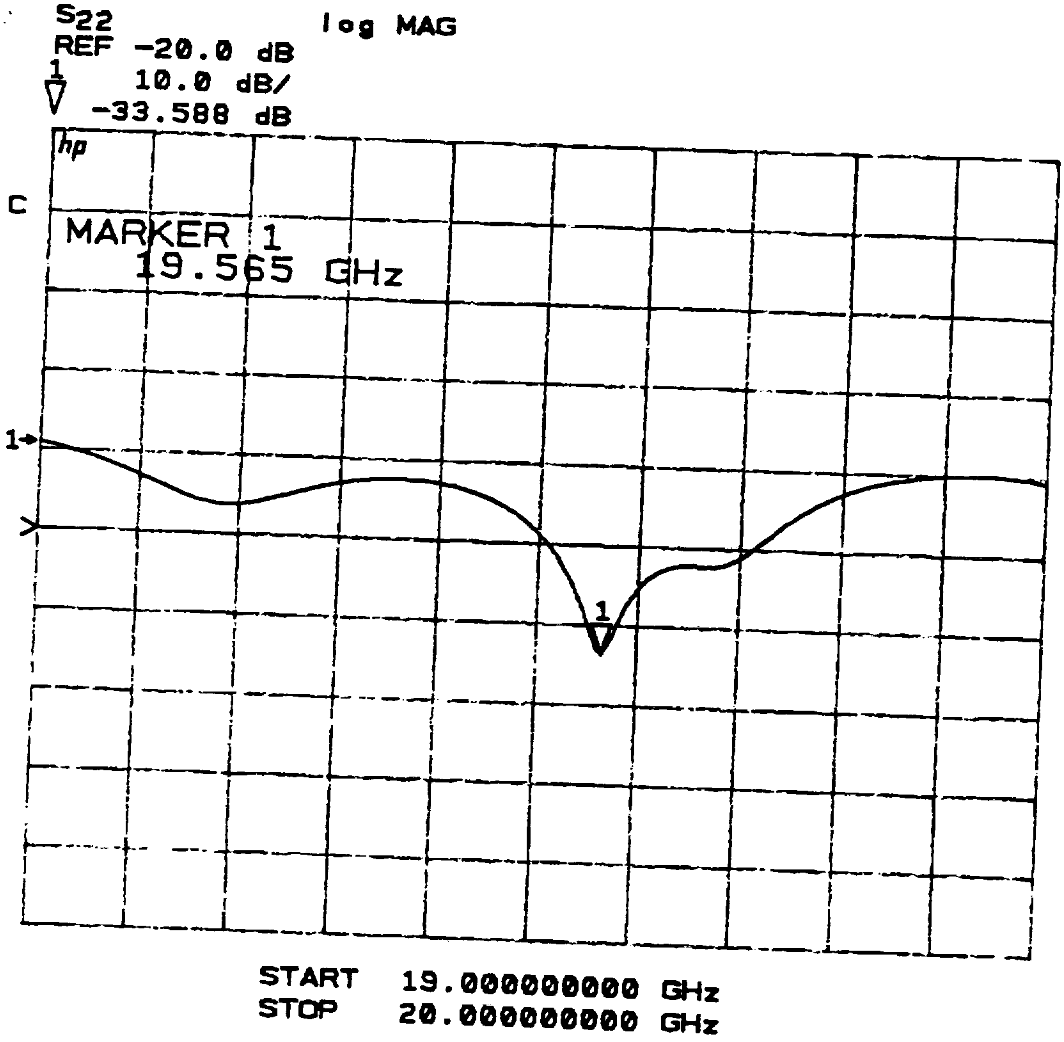

Figure 4.18: Measured magnitude of the reflection coefficient for the circularly polarized 4-element gap-coupled patch antenna array in Fig. 4.17.

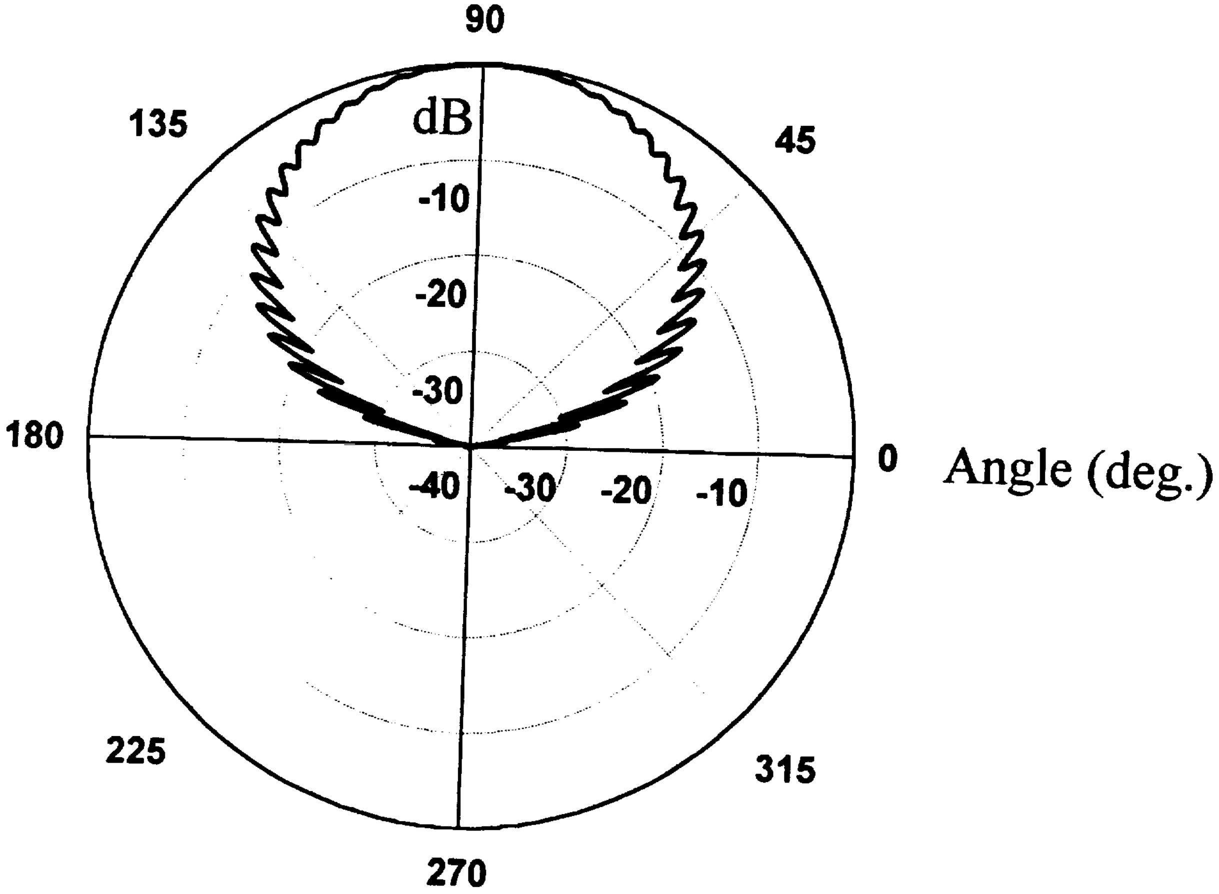

Figure 4.19: Theoretical principle plane spinning dipole pattern for the circularly polarized 4-element gap-coupled patch antenna array in Fig. 4.17.

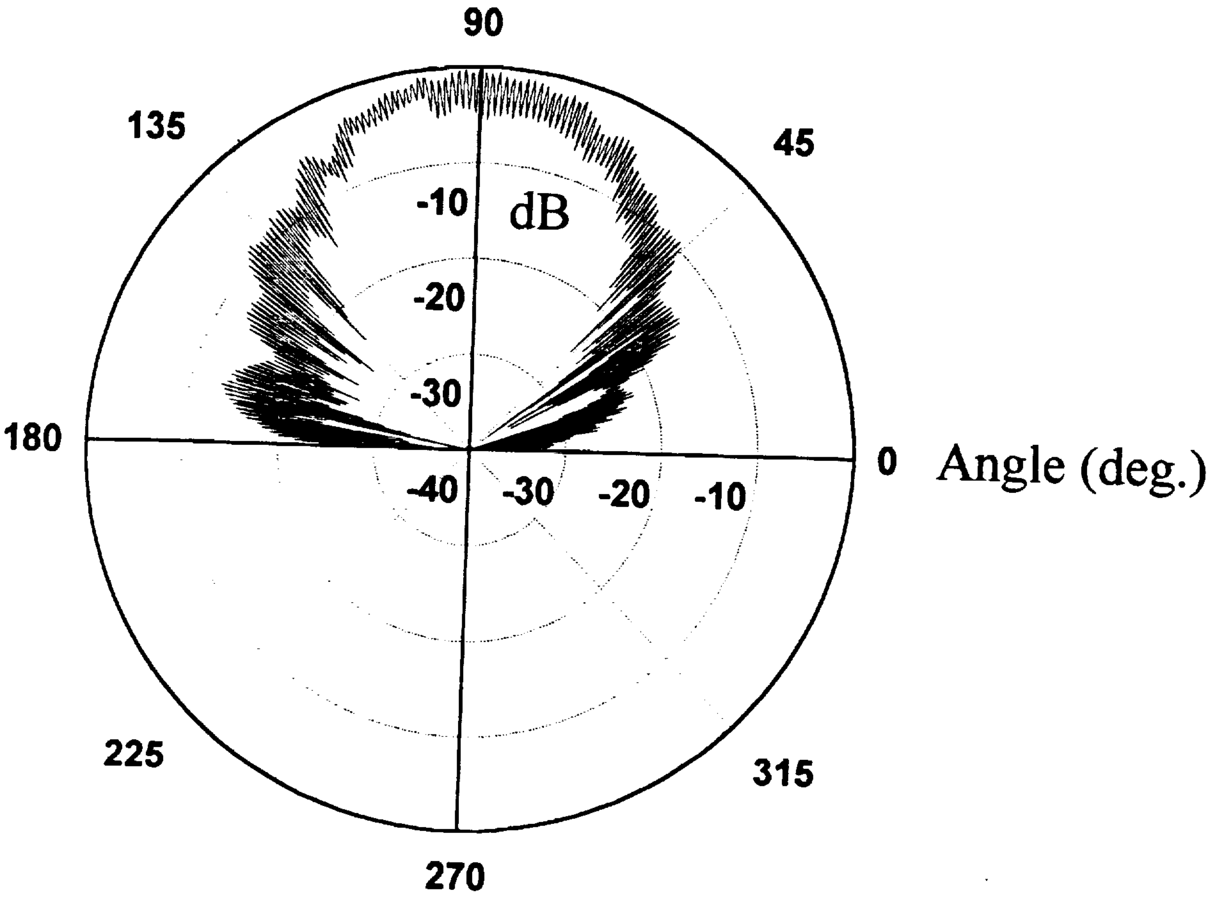

Figure 4.20: Measured principle plane spinning dipole pattern for the circularly polarized gap-coupled patch antenna in Fig. 4.17.

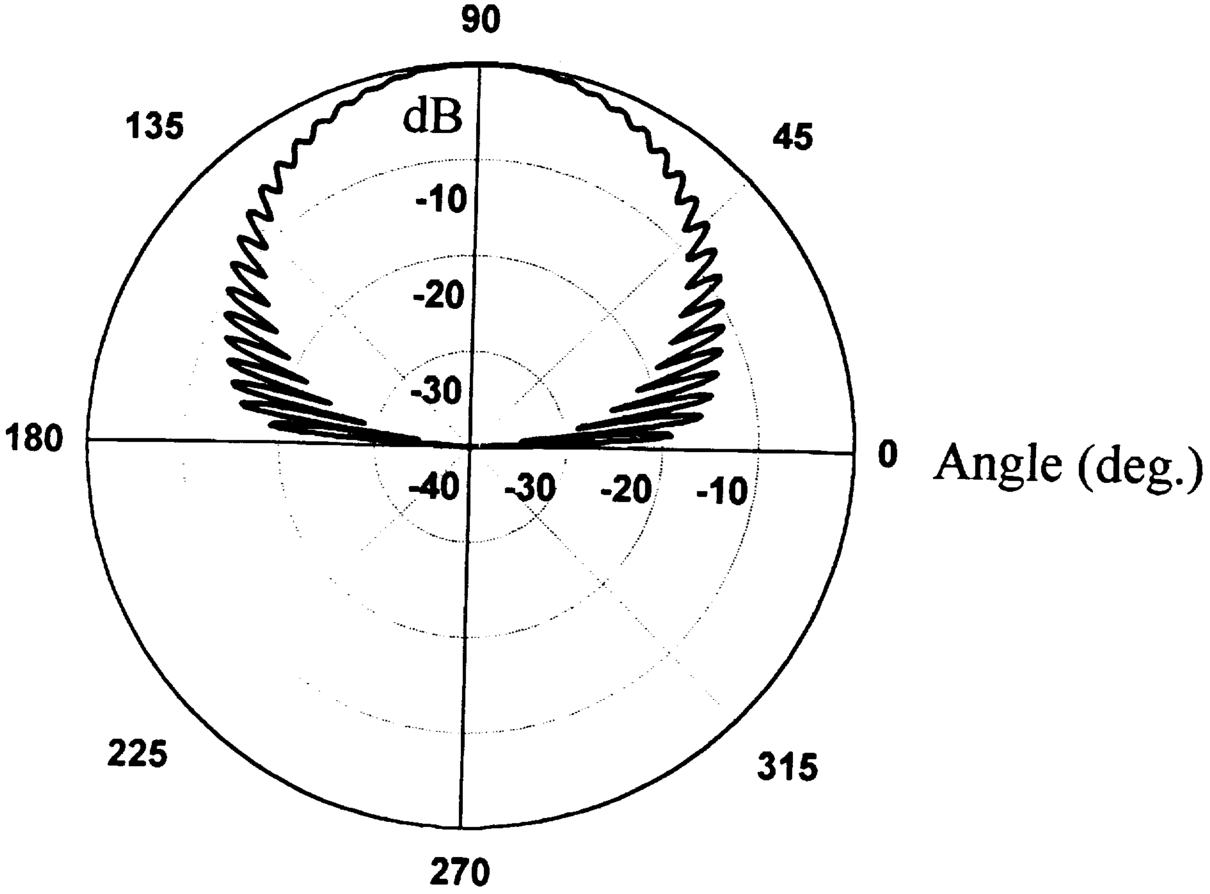

Figure 4.21: Theoretical diagonal plane spinning dipole pattern for the circularly polarized 4-element gap-coupled patch antenna array in Fig. 4.17.

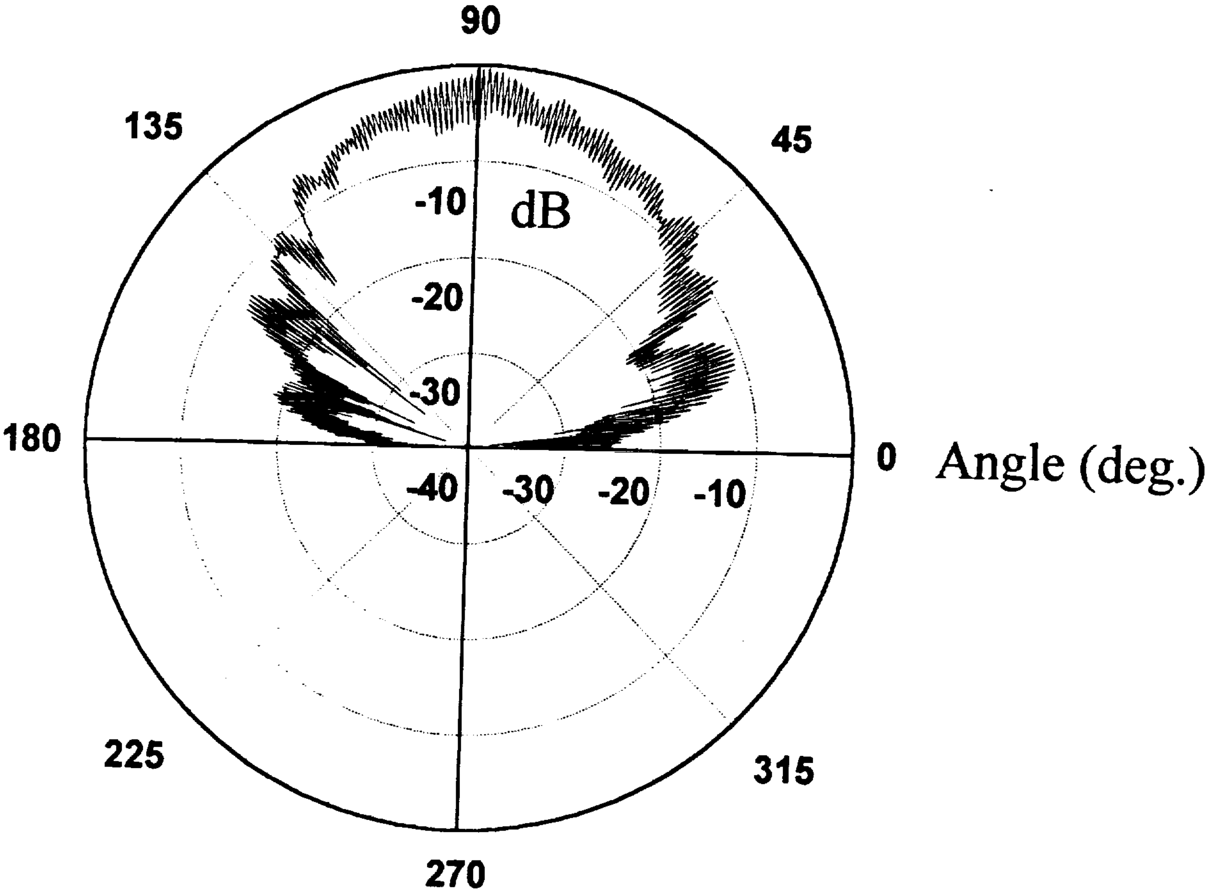

Figure 4.22: Measured diagonal plane spinning dipole pattern for the circularly polarized gap-coupled patch antenna in Fig. 4.17.

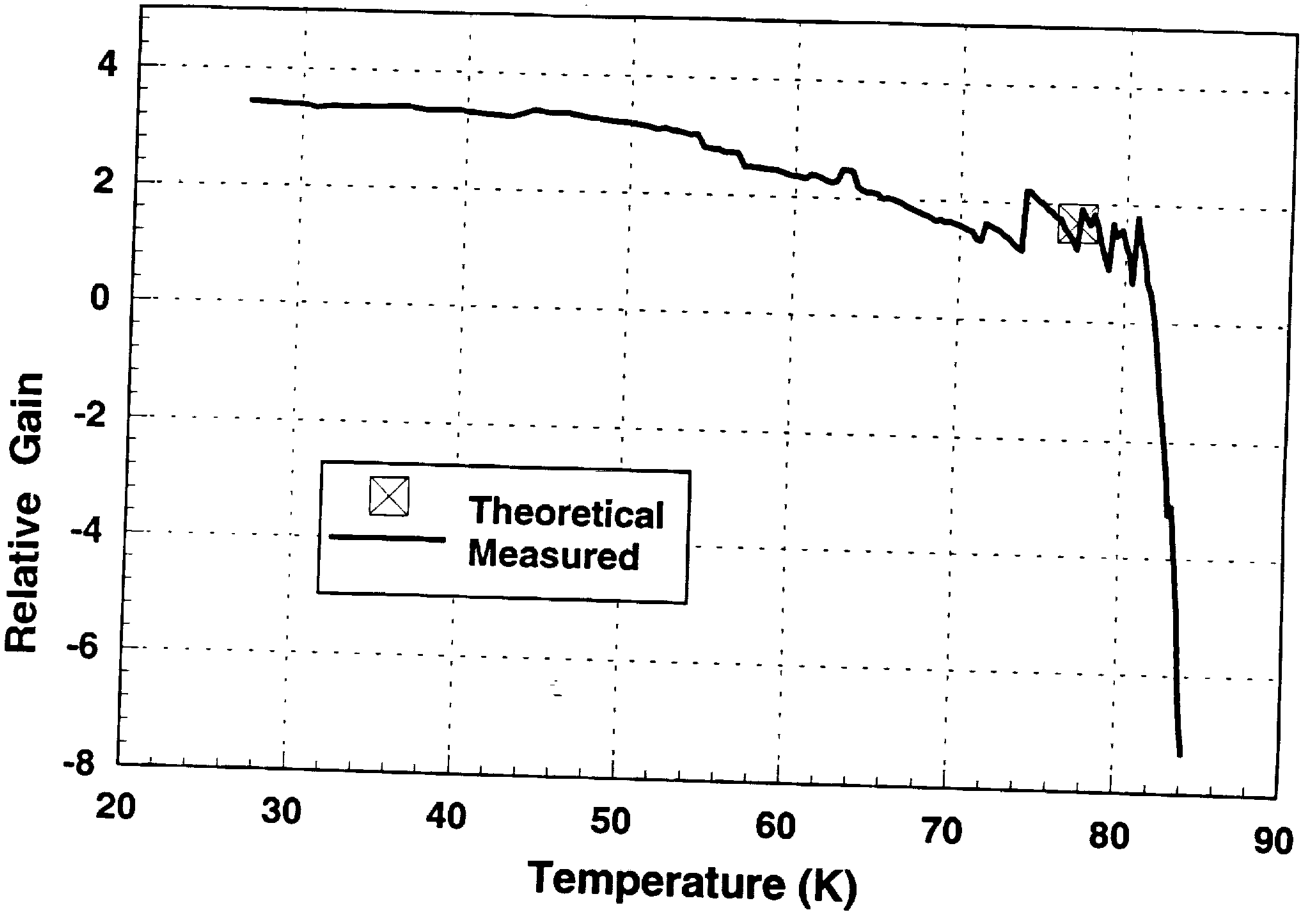

Figure 4.23: Gain of the 4-element YBCO gap-coupled array relative to the 4-element copper gap-coupled array ($300K$) as a function of temperature.

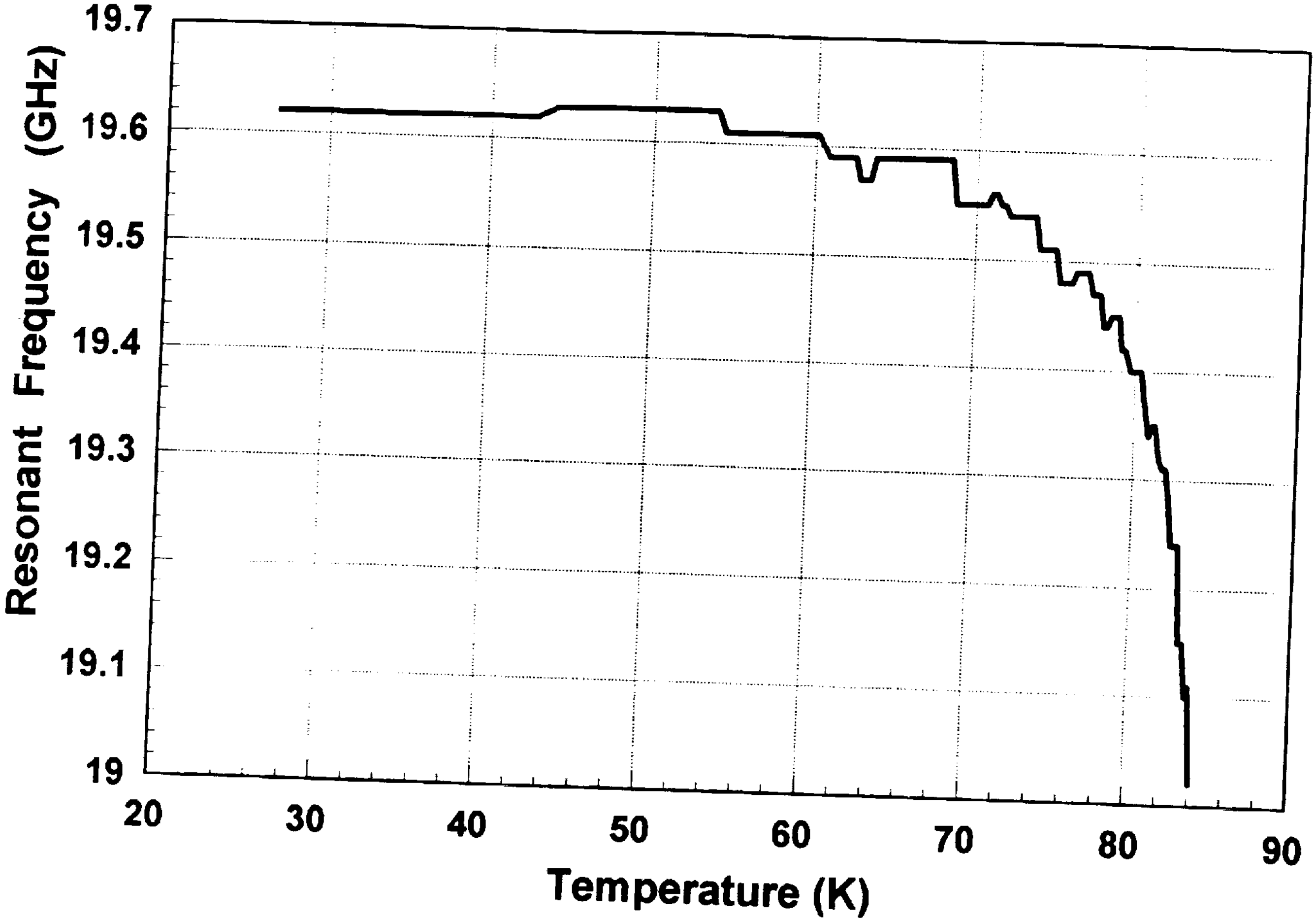

Figure 4.24: Resonant frequency of the 4-element YBCO gap-coupled array as a function of temperature.

CHAPTER 5

Summary

In large microstrip antenna arrays, superconductors are used to increase the gain of the antenna, primarily, by decreasing the loss in the microstrip transmission line feed network. In addition, when constructed from superconducting materials, the efficiency, and therefore the gain, of microstrip patches increases if the substrate is not so thick that the dominant loss mechanism for the patch is radiation into the surface waves of the conductor-backed substrate.

The primary goal of this study was to design and characterize a 4-element 20 GHz, circularly polarized microstrip patch antenna fabricated from $YBa_2Cu_3O_x$ superconductor. The purpose of the study is to support a high temperature superconductivity flight communications experiment between the Space Shuttle orbiter and the ACTS satellite. This study is intended to provide information into the design, construction, and feasibility of a circularly polarized superconducting 20 GHz downlink or cross-link antenna.

In this report we have presented analysis and discussion intended to show the effects of different conducting material on the efficiency of microstrip array antennas. We have demonstrated that significant gain improvements can be realized by using superconducting materials for large corporate fed array antennas. In addition, for thin microstrip patch elements the efficiency is increased with the use of superconductors. We have, also, reviewed some of the previous investigations into superconducting linearly polarized microstrip elements and arrays. With this information, we proceeded to describe some significant issues associated with the design of a circularly polarized HTS microstrip antenna array. In particular, we discussed some of the following aspects of using the high dielectric constant $LaAlO_3$ substrates: extreme variations in the dielectric constant, good lattice match with $YBa_2Cu_3O_x$, miniaturization and reduced bandwidth of microstrip elements on $LaAlO_3$, and high microstrip patch edge impedances.

We have considered two design configurations for a 4-element circularly polarized microstrip antenna array on this substrate. The first was the Huang array that uses properly oriented and phased linearly polarized microstrip patch elements to realize a circularly polarized pattern. The second was an array of gap-coupled circularly polarized elements. In this study we determined that although the Huang array operates well on low dielectric constant substrates, its performance becomes extremely sensitive to mismatches, inter-element coupling, and design imperfections for substrates with high dielectric constants. On $LaAlO_3$, these effects were too large to overcome, so we abandoned this design.

We had much better success with the gap-coupled microstrip array. We were able to experimentally determine the gap size necessary to achieve a good match between the feed line and the patch. Then we fabricated and tested circularly polarized elements and 4-element arrays on $LaAlO_3$ using sputtered copper films. These antennas were found to perform well, with relatively good circular polarization.

The final part of the investigation involved the realization of a 4-element superconducting antenna. Using the design established in copper, we constructed a $YBa_2Cu_3O_x$ array and measured its patterns and gain relative to the room temperature copper array. Below the transition temperature of the film, the YBCO antenna array operated well. The patterns were essentially the same as that for the copper array, with a slightly worse axial ratio due to a small amount of over etching of the superconducting circuit. The measured gain of the YBCO array was greater than that for the room temperature copper array for temperatures below $82K$. At $77K$ the relative gain was approximately equal to the predicted value of 1.67 dB and increased to 3.4 dB at $30K$.

The results of this investigation demonstrate that high temperature superconductors can be used in microstrip antenna arrays to improve their efficiency. In addition, the circularly polarized arrays can be realized using superconducting thin films on high dielectric constant substrates such as $LaAlO_3$. Obviously, not all large array applications will benefit from the use of HTS materials because of the added complexity of cryogenic cooling and the required use of high dielectric constant substrates. However, HTS materials, when incorporated in designs such as those developed in this work, do offer potential gain improvements for antenna systems that can accommodate the added constraints of the superconducting environment.

REFERENCES

[1] S.H. Talisa, M.A. Janocko, C. Moskowitz, J Talvaccio, J.F. Billing, R. Brown, D.C. Buck, C.K. Jones, B.R. McAvoy, G.R. Wagner, and D.H. Watt, "Low and high temperature superconducting microwave filters," *IEEE Trans. Microwave Theory and Tech.*, vol. 39, no. 9, pp. 1455-1461, 1991.

[2] C. Wilker, Z.Y. Shen, P. Pang, D.W. Face, W.L. Holstein, A.L. Mattews, and D.B. Laubacker, "5 GHz high-temperature superconducting resonators with high Q and low power dependence to 90K," *IEEE Trans. Microwave Theory and Tech.*, vol. 39, no. 9, pp. 1462-1469, 1991.

[3] W.G. Lyons, R.R. Bonetti, A.E. Williams, P.M. Mankiewich, M.L. O'Malley, J.M. Hamm, A.C. Anderson, R.S. Withers, A. Menlenberg, and R.E. Howard, "High Tc superconductive microwave filters," *IEEE Trans. on Magnetics*, vol. 27, no. 2, pp. 2537-2539, 1991.

[4] M.A. Richard, K.B. Bhasin, C. Gilbert, S. Metzler, G. Keopf, and P.C. Claspy, "Performance of a four-element Ka-band high temperature superconducting microstrip antenna," *IEEE Trans. Microwave and Guided Wave Letters*, vol. 2, no. 4, pp. 143-145, 1992.

[5] N.J. Rohrer, M.A. Richard, G.J. Valco, and K.B. Bhasin, "A 10 GHz Y-Ba-Cu-O/GaAs hybrid oscillator proximity coupled to a circular microstrip patch antenna," *IEEE Trans. Applied Superconductivity*, vol. 3, no. 1, pp. 23-27, 1993.

[6] M.A. Richard, K.B. Bhasin, P.C. Claspy, "Superconducting microstrip antennas: An experimental comparison of two feeding methods," *IEEE Trans. Antennas and Propagation*, vol. 41, no. 7, pp. 967-974, 1993.

✓ [7 M.R. Richard, "An experimental investigation of high temperature superconducting microstrip antennas at K- and Ka-band frequencies," NASA contractor report 191089, 1993.

[8] J.S. Herd, J.P. Kennedy, K.G. Herd, W.G. Lyons, A. Anderson, P.M. Mankiewich, and M.C. O'Malley, "Experimental results on a 12 GHz 16-element multilayer microstrip array with a high-Tc superconducting feed network," *IEEE Antennas and Propagation Symposium Digest*, pp. 974-977, 1992.

[9] J.S. Herd, D. Hayes, J.P. Kennedy, L.D. Poles, K.G. Herd, and W.G. Lyons, "Experimental results on a scanned beam microstrip antenna array with a proximity coupled YBCO feed network," *IEEE Trans. Applied Superconductivity*, vol. 2, no. 1, pp. 2840-2843, 1993.

[10] L.L. Lewis, G. Koepf, K.B. Bhasin, and M.A. Richard, "Performance of a TlCaBaCuO 30 GHz 64-element antenna array," *IEEE Trans. Applied Superconductivity*, vol. 3, no. 1, pp. 2844-2847, 1993.

[11] R.L. Smith, T.E. Harrington, J.T. Williams, and S.A. Long, "Superconducting microstrip patch antennas," *North American URSI Radio Science Meeting Digest*, p. 30, 1991.

[12] R.L. Smith, "Design and experimental characterization of a coplanar waveguide fed high temperature superconducting microstrip patch antenna," M.S. Thesis, University of Houston, Houston, TX, 1992.

[13] R.J. Dinger, D.R. Bowling, A.M. Martin, and J. Talvacchio, "Radiation efficiency measurements of a thin-film Y-Ba-Cu-O superconducting half-loop antenna at 500 MHz," *IEEE Microwave Theory and Tech. Symposium Digest*, pp. 1243-1246, 1991.

[14] R.J. Dinger, D.R. Bowling, and A.M. Martin, "A survey of possible passive antenna applications of high temperature superconductors," *IEEE Trans. Microwave Theory and Tech.*, vol. 39, no. 9, pp. 1498-1507, 1991.

[15] R.E. Collin, Foundations for Microwave Engineering, McGraw-Hill, New York, 1992.

[16] T. Van Duzer and C.W. Turner, Principles of Superconducting Devices and Circuits, Elsevier North Holland, New York, 1991.

[17] N.G. Alexopoulos and D.R. Jackson, "Fundamental superstrate (cover) effects on printed circuit antennas," *IEEE Trans. Antennas and Propagation*, vol. 32, no. 8, pp. 807-815, 1984.

[18] D.R. Jackson and N.G. Alexopoulos, "Simple formulas for the input impedance, bandwidth, and radiation efficiency of a rectangular patch," *IEEE Trans. Antennas and Propagation*, vol. 39, no. 3, pp. 407-410, 1991.

[19] R.L. Smith, J.T. Williams, S.A. Long, and J.C. Wolfe, "Design and experimental characterization of a coplanar waveguide fed high temperature superconducting microstrip patch antenna," Technical Report No. 93-12, Applied Electromagnetics Laboratory, Department of Electrical Engineering, University of Houston, 1993. (Report delivered to NASA-JSC.)

[20] D.R. Jackson and J.T. Williams, "A comparison of CAD models for radiation from rectangular microstrip patches," *International Journal of Microwave and Millimeter-Wave Computer-Aided Engineering*, vol. 1, no. 2, pp. 236-248, 1991.

[21] J. Huang, "A technique for an array to generate circular polarization with linearly polarized elements," *IEEE Trans. Antennas and Propagation*, vol. 34, no. 9, pp. 1113-1124, 1986.